

The global effects of impact-induced seismic activity on fractured asteroid surface morphology

James E. Richardson Jr.^{a,*}, H. Jay Melosh^b, Richard J. Greenberg^b, David P. O'Brien^c

^a Center for Radiophysics and Space Research, 310 Space Sciences Building, Cornell University, Ithaca, NY 14853, USA

^b Lunar and Planetary Laboratory, University of Arizona, Tucson, AZ 85721-0092, USA

^c Observatoire de Nice, Bld. de l'Observatoire, B.P. 4229, 06304 Nice Cedex 4, France

Received 12 February 2005; revised 22 June 2005

Available online 12 September 2005

Abstract

Impact-induced seismic vibrations have long been suspected of being an important surface modification process on small satellites and asteroids. In this study, we use a series of linked seismic and geomorphic models to investigate the process in detail. We begin by developing a basic theory for the propagation of seismic energy in a highly fractured asteroid, and we use this theory to model the global vibrations experienced on the surface of an asteroid following an impact. These synthetic seismograms are then applied to a model of regolith resting on a slope, and the resulting downslope motion is computed for a full range of impactor sizes. Next, this computed downslope regolith flow is used in a morphological model of impact crater degradation and erasure, showing how topographic erosion accumulates as a function of time and the number of impacts. Finally, these results are applied in a stochastic cratering model for the surface of an Eros-like body (same volume and surface area as the asteroid), with craters formed by impacts and then erased by the effects of superposing craters, ejecta coverage, and seismic shakedown. This simulation shows good agreement with the observed 433 Eros cratering record at a Main Belt exposure age of 400 ± 200 Myr, including the observed paucity of small craters. The lowered equilibrium numbers (loss rate = production rate) for craters less than ~ 100 m in diameter is a direct result of seismic erasure, which requires less than a meter of mobilized regolith to reproduce the NEAR observations. This study also points to an upper limit on asteroid size for experiencing global, surface-modifying, seismic effects from individual impacts of about 70–100 km (depending upon asteroid seismic properties). Larger asteroids will experience only localized (regional) seismic effects from individual impacts.

© 2005 Elsevier Inc. All rights reserved.

Keywords: Asteroids, composition; Asteroids, Eros; Impact processes; Regoliths; Surfaces, asteroids

1. Introduction

1.1. Background

The NEAR–Shoemaker orbiter mission to the Asteroid 433 Eros (2000–2001) revealed a heavily cratered surface, covered with a veneer of loose regolith (tens of meters thick in places) and peppered with numerous boulders (Veverka et al., 2001; Robinson et al., 2002). This regolith layer displays direct evidence of downslope movement in several

forms (see Fig. 1): slumps and debris aprons at the base of steep slopes, bright streaks of freshly exposed material on crater walls, the pooling of regolith in topographic lows, a large number of degraded craters, and a deficit of craters less than ~ 100 m in diameter as extrapolated from larger crater sizes (Veverka et al., 2001; Chapman et al., 2002; Cheng et al., 2002a; Thomas et al., 2002; Robinson et al., 2002). One proposed explanation for these phenomena is seismic reverberation of the asteroid following impact events (Veverka et al., 2001), which is potentially capable of destabilizing slopes, causing regolith to migrate downslope, and degrading or erasing small craters.

The idea that impact-produced seismic activity can modify the surface of a target body is hardly a new one. The

* Corresponding author. Fax: +1 (607) 255 9002.

E-mail address: richardson@astro.cornell.edu (J.E. Richardson Jr.).

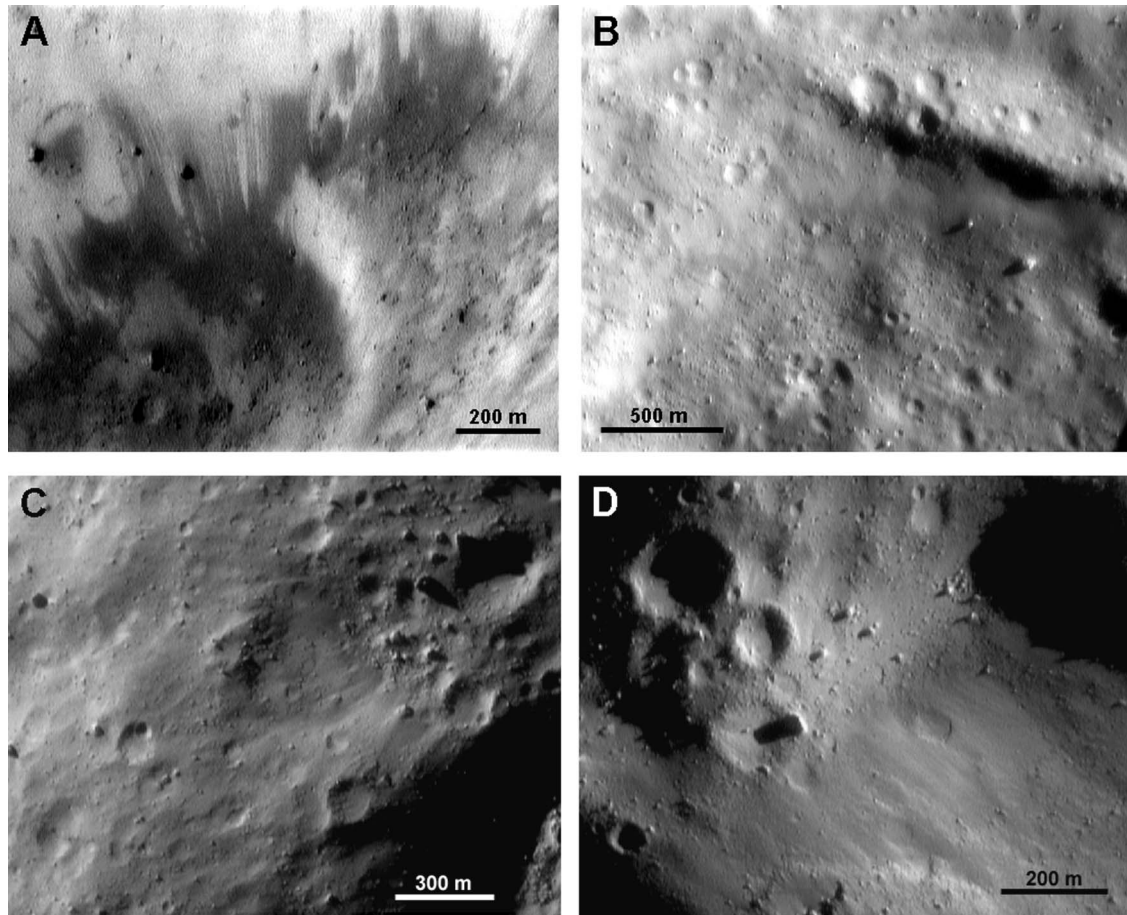


Fig. 1. Indications of downslope regolith motion on 433 Eros, imaged by the NEAR–Shoemaker spacecraft, in the form of: (A) bright streaks of freshly exposed material on a large crater wall, as the darker material moves downslope (MET 154409710, 14.79 W, 14.21 S, 2.67 m pixel⁻¹); (B) talus cones and debris avalanches emanating from a steep scarp (MET 132929106, 284.42 W, 41.31 N, 4.60 m pixel⁻¹); (C) a debris apron extending into a highly eroded crater from a rise at the top of the image, and a thick layer of regolith gently encroaching into the same crater from the bottom of the image (MET 153667920, 260.29 W, 14.89 S, 3.41 m pixel⁻¹); and (D) the collection of regolith (and scattered boulders) in topographic lows, several degraded (softened) craters, a few barely visible ‘ghost’ craters, and a general lack of small craters, particularly in the smooth areas on the right (MET 154251925, 24.81 W, 6.28 S, 2.10 m pixel⁻¹).

Ranger images of the Earth’s moon revealed downslope flow of material on lunar slopes in the form of slides, slumps, and creep processes, and impact-induced seismicity was proposed as a potential cause (Titley, 1966). Further analysis showed that while impacts large enough to produce complex craters and basins can produce widespread seismic effects on the Moon (Schultz and Gault, 1975a, 1975b), the impacts that form small, simple craters will affect only localized areas of high slope (Houston et al., 1973). The Mariner and Viking images of the martian moons, Phobos and Deimos, opened up this same question with regard to small satellites and asteroids. J. Arnold is given credit for first suggesting that the downslope movement of regolith could be an important surface process on asteroids, despite the tiny surface gravitational fields on these small bodies (Chapman, 1978). In the same year, Cintala et al. (1978) published two of the primary reasons why impact-induced seismic shaking of a small body is an attractive surface modification mechanism. First, the small volume of the body keeps the concentration of seismic energy high even after the seismic energy

injected by an impact has completely dispersed throughout the target body. Second, the very low surface gravity of a small body ($g_a < 10^{-3} g_{\text{Earth}}$) permits relatively small seismic accelerations to destabilize material resting on slopes, where destabilization begins at 0.2–0.5 g_a for loose regolith (Lambe and Whitman, 1979).

Modeling of the elastic stresses and seismic effects of large impacts on small bodies began with the work of Fujiwara (1991) and Ivanov (1991), who investigated the formation of the Stickney impact basin on Phobos and the resulting stress features on its surface. In a separate analysis, Asphaug and Melosh (1993) performed hydrocode modeling of the impact that produced the Stickney basin, and as a by-product estimated the resulting velocities imparted to a hypothetical regolith layer resting on the surface of the small satellite, along with approximate ballistic travel distances: an effect called seismic ‘jolt’ (Nolan et al., 1992). Asphaug and Melosh (1993) thus produced the first published computation of impact seismic effects on the regolith layer of a small body. Following up on this method, M. Nolan pro-

duced more extensive seismic jolt estimates for the surfaces of Asteroid 951 Gaspra (Greenberg et al., 1994) and 243 Ida (Greenberg et al., 1996), which were imaged at close range by the Galileo spacecraft in 1991 and 1993, respectively. These analyses indicated that impacts producing kilometer-sized craters on these small asteroids can have severe effects on their cratering records, erasing most of the craters below a few hundred meters in diameter when a thick, loose regolith layer exists. Further three-dimensional modeling using an Ida shape model demonstrated how severe antipodal surface damage (such as groove formation) can result from large impacts, even when the target body has a highly irregular shape (Asphaug et al., 1996).

In this study, we will use the high-resolution, global-coverage, 433 Eros data set returned by the NEAR–Shoemaker spacecraft to provide us with important modeling constraints in investigating the phenomena of impact-induced seismic shaking on fractured, stony asteroids in the 10–100 km size range; such that any adequate model of impact generated seismic effects must be able to explain and match this observational evidence. In addition to the more obvious indications of downslope regolith motion, we will pay particular attention to the Eros cratering record, especially the large number of degraded craters and the paucity of small craters (see Chapman et al. (2002) for size-frequency distribution plots and discussion).

1.2. Minimum impactor size for global seismic effects (I)

Why is seismic shaking an attractive mechanism for small asteroids? We can illustrate both points raised by Cintala et al. (1978) (above) by equating the seismic energy injected by an impactor, which is a small fraction of the impactor's kinetic energy, with the seismic energy necessary to produce accelerations that exceed the asteroid's surface gravity g_a throughout its volume, and therefore destabilize all slopes on the surface. This calculation will give us an analytical estimate of the minimum diameter of impactor necessary to cause global seismic effects on the surface of a target asteroid.

The seismic energy injected by an impactor E_i is given by:

$$E_i = \eta E_k = \frac{1}{12} \eta \pi \rho_p v_p^2 D_p^3, \quad (1)$$

where η is an impact seismic efficiency factor (addressed in further detail below), E_k is the kinetic energy of an impactor, ρ_p is the mean projectile density, v_p is the impact velocity, and D_p is the spherical projectile diameter. Equation (1) gives us one half of our desired expression.

The average seismic strain energy per unit volume of rock ϵ_d (energy density), expressed in terms of the maximum half-cycle amplitude A resulting from a single (primary) seismic frequency is derived in Lay and Wallace (1995) as:

$$\epsilon_d = \pi^2 \rho_a \frac{A^2}{\tau^2}, \quad (2)$$

where ρ_a is the mean density of the asteroid and τ is the period of the seismic waves. Placing Eq. (2) in terms of the seismic frequency in Hertz f rather than period τ gives:

$$\epsilon_d = \rho_a \pi^2 f^2 A^2. \quad (3)$$

Since the maximum acceleration a experienced by the medium can be expressed as a function of the maximum displacement A and frequency f ($a = -4\pi^2 f^2 A$), we can rewrite Eq. (3) in these terms:

$$\epsilon_d = \frac{\rho_a a^2}{16\pi^2 f^2}. \quad (4)$$

Equation (4) gives us an expression for the strain (potential) energy density in the system. Similar to a harmonic oscillator, the total energy in the system is equally divided between potential and kinetic energy (Lay and Wallace, 1995). Therefore, we can express the total seismic energy density in the system as $\epsilon_s = 2\epsilon_d$, giving:

$$\epsilon_s = \frac{\rho_a a^2}{8\pi^2 f^2}. \quad (5)$$

Equation (5) thus provides us with a method for expressing the total seismic energy density ϵ_s in terms of the maximum acceleration a imparted to the rock. Therefore, equating a with the gravitational acceleration g_a on the surface of a spherical asteroid, and then multiplying ϵ_s by the volume of this spherical asteroid gives us the total amount of seismic energy E_s necessary to produce 1 g_a accelerations throughout the asteroid volume:

$$E_s = \frac{1\pi G^2 \rho_a^3 D_a^5}{108 f^2}, \quad (6)$$

where G is the gravitational constant and D_a is the asteroid diameter. Equation (6) gives us the other half of our desired expression.

We now equate E_i (Eq. (1)) with E_s (Eq. (6)) and solve for the diameter of a stony projectile D_p which meets this condition as a function of asteroid diameter D_a , yielding:

$$D_p = \left[\frac{G^2 \rho_a^3 D_a^5}{9\eta \rho_p v_p^2 f^2} \right]^{1/3}. \quad (7)$$

Fig. 2 shows a plot of Eq. (7), giving the minimum impactor diameter D_p necessary to cause global seismic effects on an asteroid of diameter D_a for three different seismic frequencies, using a typical asteroid impact speed of $v_p = 5 \text{ km s}^{-1}$ (Bottke et al., 1994), asteroid density of $\rho_a = 2700 \text{ km m}^{-3}$ (near the Eros value of $2670 \pm 30 \text{ km m}^{-3}$ (Yeomans et al., 2000)), projectile density of $\rho_p = 2500 \text{ km m}^{-3}$, and impact seismic efficiency of $\eta = 10^{-4}$ (Schultz and Gault, 1975a; Melosh, 1989). Also shown is the minimum impactor diameter D_p necessary to cause the disruption of an asteroid of diameter D_a (loss to space of $>50\%$ of the asteroid's mass), using the formulae given in Melosh and Ryan (1997) and Benz and Asphaug (1999), respectively. The region bounded by these

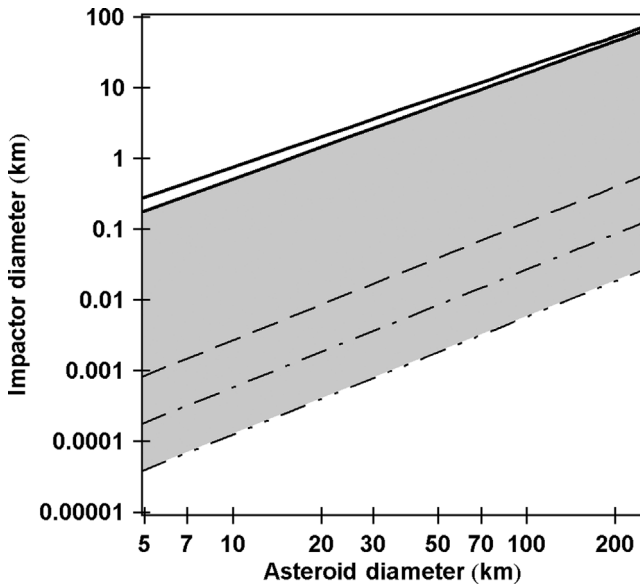


Fig. 2. (Lower curves) Minimum stony impactor diameter necessary to cause $1 g_a$ accelerations throughout the volume of a stony asteroid of given diameter (destabilizing all regolith-covered slopes on the surface), for seismic frequencies f of 1 Hz (dashed), 10 Hz (dot-dashed), and 100 Hz (dot-dot-dashed). (Upper solid curves) Minimum stony impactor diameter necessary to cause disruption of a stony asteroid of given diameter, calculated per Melosh and Ryan (1997) (top), and Benz and Asphaug (1999) (bottom). The region bounded by these curves, shown in gray, highlights the wide range of impactor sizes that can cause global seismic effects on an asteroid without disrupting it. This plot, however, does *not* include the important effect of seismic attenuation as the energy propagates throughout the asteroid volume.

two sets of curves (shown in gray) suggests the plausibility of a broad range of impactor sizes that can produce global seismic effects without disrupting the target asteroid. For an asteroid the size of Eros (mean diameter $D_a \approx 17$ km) the minimum impactor diameter necessary to achieve global seismic accelerations of $1 g_a$ is quite small, $D_p \approx 2$ m (0.5–10 m): far smaller than the size of impactor that would disrupt the asteroid: $D_p \approx 1.1$ km (Melosh and Ryan, 1997), $D_p \approx 1.6$ km (Benz and Asphaug, 1999). These plots are rather simplistic, however, because the important effect of seismic energy attenuation is not included. We will therefore revisit this analytical calculation further on in this study.

The impact seismic efficiency factor η , the fraction of the impactor's kinetic energy that is ultimately converted to seismic energy within the target body, is an important, but poorly constrained parameter. Various values from the literature include:

- Gault and Heitowit (1963) report an upper limit of 10^{-2} for small laboratory impacts.
- Titley (1966) reports 3×10^{-1} to 3×10^{-3} for nuclear and other large explosion sources.
- McGarr et al. (1969) report 10^{-4} to 10^{-6} from laboratory experiments.

- Latham et al. (1968) report 1×10^{-5} to 5×10^{-5} from White Sands missile impact tests.
- Latham et al. (1968) report 10^{-5} to 10^{-6} for low angle Lunar Module impacts on the Moon.
- Schultz and Gault (1975a) estimate 10^{-3} to 10^{-5} from various sources.

As listed above, the Saturn IVB booster and Lunar Module (LM) impacts performed as part of the Apollo Passive Seismic Experiment (PSE) gave values of η between 10^{-5} and 10^{-6} (Latham et al., 1968; Toksoz et al., 1974). However, only the long-period (LP) seismometers were used for these determinations, which had an upper frequency limit of about 1 Hz (Toksoz et al., 1974). As will be shown in Section 2, the peak seismic frequencies produced by an impact are higher, generally falling within the range of 5–50 Hz. Consequently, the lunar impact determinations of η sampled only the low-frequency, low-energy ‘wing’ of the impact seismic signal power spectrum, and we thus adopt $\eta = 10^{-6}$ as a loose lower limit on η in our modeling. On the other hand, Schultz and Gault (1975a) adopted $\eta = 10^{-4}$ for large impacts, and this value is also given as a typical value for most impacts by Melosh (1989). We will therefore utilize two values for this constant in this work: (1) following previous precedent we adopt $\eta = 10^{-4}$ as our ‘typical’ value, but (2) we will also investigate the more restrictive case of $\eta = 10^{-6}$.

1.3. Determining the surface effects of seismic shaking

In Section 1.2 we demonstrated the availability of sufficient seismic energy from even modest-sized impactors for producing global seismic effects on an asteroid less than 200 km in diameter, but a much more detailed analysis is required to quantify this effect as a surface modification process. The precursor for this work is a classic study of the seismic effect of impacts on lunar surface topography, performed by Houston et al. (1973). Building upon these earlier techniques, we investigate the seismic modification process through three modeling phases: seismic modeling (Section 2), geomorphic modeling (Section 3), and impact cratering statistics modeling (Section 4). In Section 2, we develop a basic seismic theory for fractured asteroids, find the typical seismic frequencies generated by an impact, and then use these to synthesize generic impact seismograms for a test case asteroid (433 Eros). In Section 3, we compute the mechanical response of regolith-covered slopes to impact-induced seismic vibrations, and then apply this computed downslope flow to a morphological model of the degradation and erasure of impact craters. As an application, in Section 4 we use this crater degradation model in a stochastic cratering simulation which reproduces the statistics of the cratering record on the surface of 433 Eros and shows how seismic shakedown results in the observed abundance of ‘softened’ craters and deficit of small impact craters.

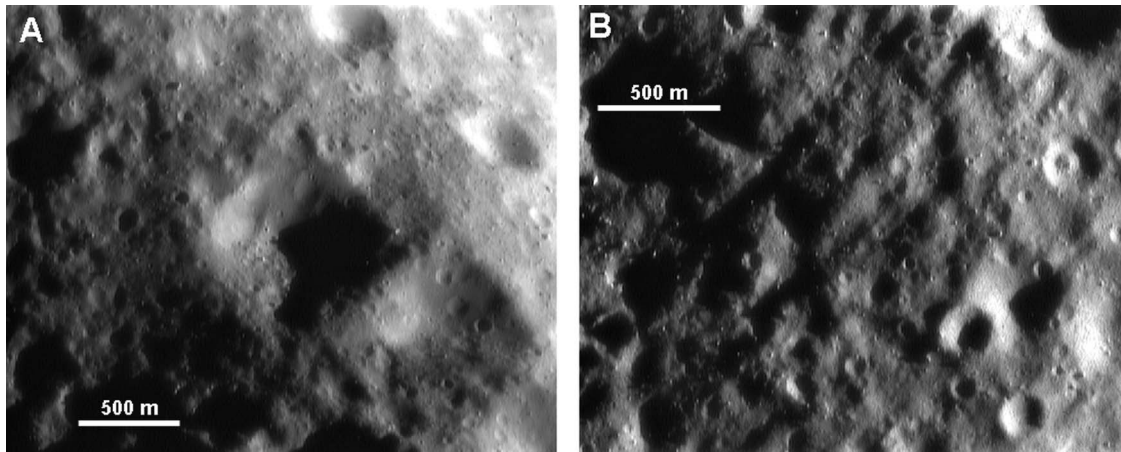


Fig. 3. Two examples of evidence for a joint and fracture structure underlying the regolith layer on 433 Eros, imaged by the NEAR–Shoemaker spacecraft, in the form of: (A) several structurally controlled, ‘square’ impact craters (MET 132151598, 218.91 W, 16.64 S, 5.57 m pixel^{−1}); and (B) a network of criss-crossing ridges and grooves, with a few, small, structurally controlled craters (MET 136266921, 218.72 W, 42.00 N, 4.58 m pixel^{−1}).

2. Seismic modeling

2.1. Seismic energy dispersion in a fractured medium

The Galileo images of 951 Gaspra and 243 Ida revealed two battered objects, with visible systems of ridges and grooves on their surfaces, several large concavities (many presumed to be from impacts (Greenberg et al., 1994, 1996), and highly irregular shapes indicative of at least some degree of structural strength (Belton et al., 1992, 1996; Carr et al., 1994; Sullivan et al., 1996). Rather than being single stone monoliths or highly pulverized ‘rubble piles,’ these features suggest that these asteroids are something in between. Further work has characterized an entire spectrum of asteroid structural types, called ‘gravitational aggregates’ by Richardson et al. (2002), which span the extremes from monolith to highly comminuted rubble pile. Britt et al. (2002) further identified a transition group in the central region of this spectrum, called ‘fractured monoliths’ or ‘fractured asteroids,’ and placed 951 Gaspra and 243 Ida into this transitional category based upon porosity estimates.

The NEAR–Shoemaker observations of 433 Eros likewise showed an asteroid that most likely falls into this transitional category of fractured monolith, based upon several lines of supporting evidence (see Fig. 3):

- Indications of structural control of impact craters and other features (Prockter et al., 2002).
- The presence of a global network of visible joints, ridges, and grooves (Zuber et al., 2000; Prockter et al., 2002).
- A mean porosity measurement of about 20–30%, consistent with a fractured rock composition (Wilkison et al., 2002; Britt et al., 2002).
- A center-of-figure to center-of-mass distance of only 30–60 m; indicative of a relatively homogeneous struc-

ture, without large-scale heterogeneities. That is, the measured porosity is likely *not* due to huge void spaces (which would probably be asymmetrical in distribution), but is instead most likely due to a homogeneous fracture and/or pore-space distribution (Thomas et al., 2002).

- A highly irregular shape, indicative of some inherent structural strength (Thomas et al., 2002; Robinson et al., 2002).

While describing the geology of 243 Ida, Sullivan et al. (1996) suggested a likely similarity between the internal structure of a fractured S-type (stony) asteroid and the uppermost crustal layers of the Earth’s moon (Dainty et al., 1974; Toksoz et al., 1974; Nakamura, 1976). Both are composed of silicate rock, presumably began as monolithic structures, and have since been exposed to impactor fluxes of similar power-law distribution for millions to billions of years—albeit of different overall magnitudes (Ivanov et al., 2002). This similarity should produce similar fracture structures within each, consisting of (see Fig. 4): (1) a thin, comminuted regolith layer on the surface, (2) a highly fractured mixture of rock and regolith beneath (a ‘megaregolith’ layer), and (3) a decreasing gradient of fractured bedrock below (Sullivan et al., 1996). In the case of the upper lunar crust, this fracture structure extends to depths of about 20–25 km (Dainty et al., 1974; Toksoz et al., 1974), but in the case of asteroids the size of Gaspra, Eros, and Ida, this fracture structure should extend throughout the body.

This type of structure provides us with an advantage in modeling the seismicity of fractured asteroids, in that the seismic behavior of the upper lunar crust in response to impacts was well characterized during the Apollo era (see Fig. 5). These lunar seismic studies showed that the dispersion of seismic energy in a fractured, highly scattering medium is a diffusion process. Therefore, the seismic energy density ϵ_s at a given location within a fractured asteroid should obey the equation (Dainty et al., 1974;

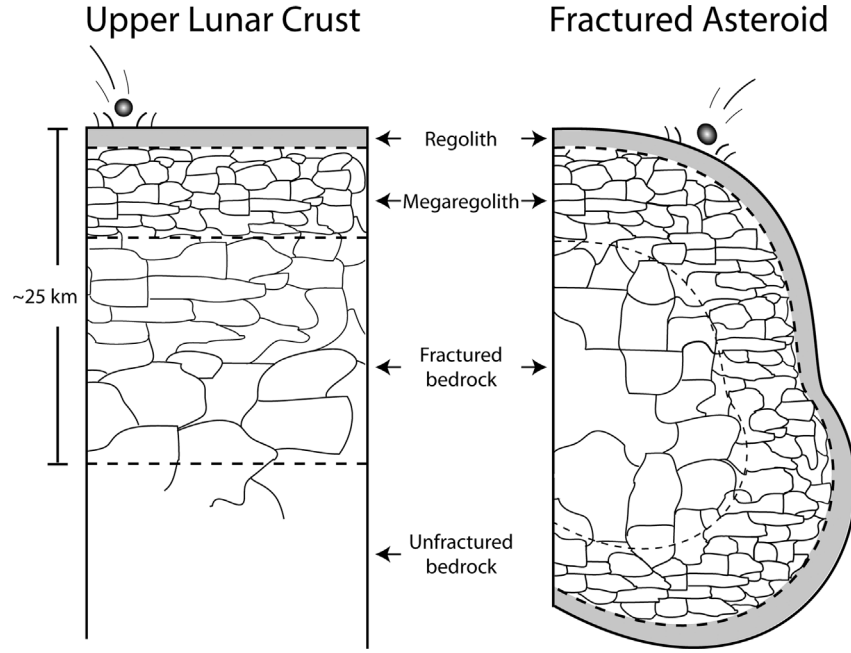


Fig. 4. Schematic view of the analogy between the upper lunar crust (investigated via the Apollo seismic experiments) and a proposed fractured asteroid structure (Sullivan et al., 1996). If each began as monolithic rock, exposure to similar impactor populations should produce similar fracture structures within each: (1) a thin, comminuted regolith layer on the surface; (2) a highly fractured mixture of rock and regolith beneath (a ‘megaregolith’ layer); and (3) a decreasing gradient of fractured bedrock below. In the case of the upper lunar crust, this fracture structure extends to depths of about 20–25 km (Dainty et al., 1974; Toksoz et al., 1974), but in the case of asteroids, this fracture structure should extend throughout the body. Based on Fig. 4 of Dainty et al. (1974).

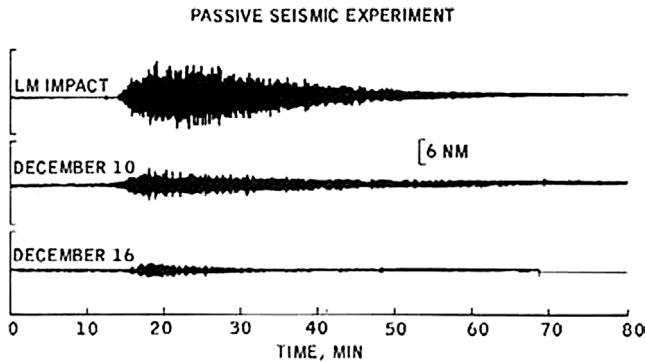


Fig. 5. Examples of one artificial and two natural impact seismograms recorded by the Apollo 12 seismic experiment (ALSEP) long-period (LP) instrument in 1969. Note the smooth, teardrop-shaped, seismic amplitude envelopes indicative of a diffusion process, and the long ‘coda’ tails (long duration vibrations) indicative of an extremely low seismic attenuation rate—primarily due to a near zero moisture content and vacuum conditions. Based on Fig. 2 of Latham et al. (1970).

Toksoz et al., 1974):

$$\frac{\partial \epsilon_s}{\partial t} = K_s \nabla^2 \epsilon_s - \frac{2\pi f \epsilon_s}{Q}, \quad (8)$$

where t is the time, K_s is the seismic diffusivity (in $\text{m}^2 \text{s}^{-1}$), and Q is the seismic quality factor (seismic attenuation parameter).

We solve Eq. (8) in Cartesian coordinates for a rectangular target body of length L , width W , and height H . We also approximate the initial seismic energy distribution (injected by an impactor) as a delta function: reasonable because the

impactor sizes considered here are much smaller than the target asteroid. This leads to the particular solution:

$$\begin{aligned} \epsilon_s(x, y, z, t) &= e^{-2\pi f t / Q} \left[1 + 2 \sum_{n=1}^{\infty} \cos \frac{n\pi x_o}{L} \cos \frac{n\pi x}{L} e^{-K_s n^2 \pi^2 t / L^2} \right] \\ &\times \left[1 + 2 \sum_{n=1}^{\infty} \cos \frac{n\pi y_o}{W} \cos \frac{n\pi y}{W} e^{-K_s n^2 \pi^2 t / W^2} \right] \\ &\times \left[1 + 2 \sum_{n=1}^{\infty} \cos \frac{n\pi z_o}{H} \cos \frac{n\pi z}{H} e^{-K_s n^2 \pi^2 t / H^2} \right], \quad (9) \end{aligned}$$

where the impact occurs at point x_o, y_o, z_o (logically, a point on the surface should be chosen).

If the impact occurs at the origin (one corner of the target body) and the seismic receiver is placed at point L, W, H (the opposite corner of the target body), and we further let the asteroid shape be cubical, such that $W = L$ and $H = L$ (where L is the cubed root of the asteroid’s volume), Eq. (9) collapses to:

$$\epsilon_s(t) = e^{-2\pi f t / Q} \left[1 + 2 \sum_{n=1}^{\infty} (-1)^n e^{-K_s n^2 \pi^2 t / L^2} \right]^3, \quad (10)$$

for the normalized energy density as a function of time, seen on one corner of the cube from an impact on the opposite corner. This is in good agreement with the two-dimensional solutions described in Carslow and Jaeger (1959) and Toksoz et al. (1974). The normalization scheme

chosen here lets the seismic energy density ϵ_s go to 1.0 as time goes to infinity when no attenuation is present.

It may seem overly simplistic to use a cubical asteroid shape to represent an irregularly shaped asteroid such as Eros (like the proverbial, spherical-cow model). However, our purpose here is to obtain a *generic*, globally representative, ‘far-side,’ seismic energy solution, using an impact-to-receiver distance of $\sqrt{3}L$: between that of the long-axis and short-axis lengths of the actual asteroid, but still having the correct asteroid volume into which the seismic energy is dispersed. Since the goal of this study is to characterize the less severe ‘global’ effects of seismic shaking (*without* looking at enhanced vibrations closer to an impact site or looking for focusing effects due to the asteroid’s irregular shape), the Cartesian solution was determined to be adequate.

In Eqs. (9) and (10) the key propagation parameters are the seismic diffusivity K_s and the seismic quality factor Q . The seismic diffusivity is defined as (Dainty et al., 1974; Toksoz et al., 1974):

$$K_s = \frac{1}{3} v_s l_s, \quad (11)$$

where v_s is the seismic P-wave velocity in competent rock, and l_s is the mean free path for the scattering of seismic waves; that is, the distance over which $1/e$ of the seismic energy is scattered. The seismic velocity v_s is determined by the rock’s elastic properties, and the mean free path for scattering l_s is directly proportional to the mean fracture spacing within the asteroid. To adopt reasonable assumptions for each, we use values consistent with the upper lunar crust (determined from the lunar seismic experiments): a competent rock seismic velocity of $v_s = 3 \text{ km s}^{-1}$, and a range of mean free paths for scattering of $l_s = 0.125\text{--}2.000 \text{ km}$ (Dainty et al., 1974; Toksoz et al., 1974).

The seismic quality factor Q deserves special attention because of its unusual history with regard to the lunar case. Initial analysis of Moon rocks returned by the Apollo astronauts showed rather typical values for Q , on the order of a few hundred or so (Tittmann, 1977). At the same time, the lunar seismic experiments showed extremely high values for Q (Pandit and Tozer, 1970). The difference was reconciled by a series of experiments described in Tittmann (1977) and Tittmann et al. (1980)—among other papers by this group—which showed that under conditions of increasing vacuum and extremely low moisture content, many rocks (including the lunar samples) display an exponentially increasing seismic quality factor Q (decreasing seismic attenuation) up to the values determined by the lunar seismic experiments. Because S-type asteroids, such as Eros, are likewise composed of silicate rock, reside in a vacuum, and have extremely low moisture contents, we adopt lunar-like seismic quality factors in our modeling. The values of Q published for the upper lunar crust fall into two ranges: $Q = 3000\text{--}5000$ based upon data from the long-period (LP) instruments (Dainty et al., 1974; Toksoz et al., 1974), and $Q = 1600\text{--}2300$ based upon data from the short-period (SP) instruments (Nakamura, 1976). The difference

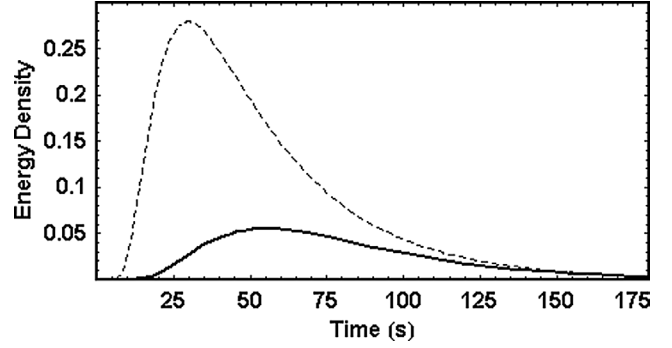


Fig. 6. A plot of the normalized seismic energy density for 3 min following an impact for (dotted) an impact and receiver located in the centers of perpendicular faces on a cubical target, using Eq. (9); and (solid) an impact and receiver located on opposite corners of a cubical target, using Eq. (10). Note the transient seismic energy peak in the dotted curve as compared to the gentle build-up and decay of seismic energy shown in the solid curve.

in these values is related to different propagation distances, propagation depths, and frequency bands used in the two studies (seismic energy leakage *underneath* the fractured zone also plays a role). We therefore cautiously adopt values of $Q = 1000\text{--}2000$ in our asteroid modeling, given that a Q of 2000 represents a rough lower limit to the actual Q of the uppermost lunar crustal layers (Nakamura, 1976).

Applying these assumed values, Fig. 6 plots the seismic energy density as a function of time for (dotted) an impact and receiver located in the centers of perpendicular faces on a cubical target body (using Eq. (9)) and (solid) an impact and receiver located on opposite corners of a cubical target body (using Eq. (10)). These solutions employ an Eros volume of $2535 \pm 20 \text{ km}^3$ (Robinson et al., 2002) which gives $L = 13.64 \text{ km}$ and an opposing-corner, impact-to-receiver distance of $\sqrt{3}L = 23.62 \text{ km}$. Comparing this value for L to the actual mean diameter of Eros, $16.92 \pm 0.04 \text{ km}$ (Robinson et al., 2002) indicates that Eq. (10) thus yields energy profiles that are *lower* than what we would obtain using the actual mean diameter of the asteroid, giving us a reasonably conservative generic solution.

2.2. Minimum impactor size for global seismic effects (II)

An examination of Eq. (10) shows two exponential terms: one for the build-up of seismic energy (as seen from the receiver), $e^{-K_s n^2 \pi^2 t / L^2}$, and one for the attenuation of seismic energy, $e^{2\pi f t / Q}$. These two terms provide us with a means for adding an estimate for seismic energy propagation-time and attenuation into our previous expression (Eq. (7)) for the size of an impactor capable of producing global surface modification on a target asteroid.

An approximation for the amount of time necessary for seismic energy to propagate from one side of an asteroid to the other can be found by finding the time at which the seismic energy build-up term from Eq. (10) goes to e^{-1} for the lowest spatial wave number n . That is, we find the ‘e-folding’ time constant for the expression, giving us a rough

estimate of the time required for the *first* (and strongest) seismic waves from the impact to reach the far side of the asteroid. This yields:

$$t = \frac{L^2}{K_s \pi^2}. \quad (12)$$

Next, we substitute this time t into the seismic energy attenuation term from Eq. (10), obtaining an estimate for the amount of seismic attenuation that occurs over the course of propagating from one side of the asteroid to the other. This gives:

$$A_s = e^{(-2\pi f L^2)/(K_s \pi^2 Q)}, \quad (13)$$

where A_s is our attenuation estimate.

We can now modify Eq. (1) to solve for the size of impactor necessary to produce $1 g_a$ accelerations on the ‘far-side’ of a target asteroid, correcting for seismic attenuation. Multiplying Eq. (1) by A_s gives:

$$E_i = \eta E_k = \frac{1}{12} \eta \pi \rho_p v_p^2 D_p^3 e^{(-2\pi f D_a^2)/(K_s \pi^2 Q)}, \quad (14)$$

where L has been replaced by the diameter of our target asteroid D_a .

Equating this new E_i with the E_s from Eq. (6) as before yields:

$$D_p = e^{(2\pi f D_a^2)/(K_s \pi^2 Q)} \left[\frac{G^2 \rho_a^3 D_a^5}{9 \eta \rho_p v_p^2 f^2} \right]^{1/3}. \quad (15)$$

Fig. 7 plots Eq. (15), showing the minimum impactor diameter D_p necessary to cause global seismic effects on an asteroid of diameter D_a for three different seismic frequencies, and using the same parameters listed in Section 1.2 along with a seismic diffusivity of $K_s = 0.250 \text{ km}^2 \text{ s}^{-1}$, and a seismic quality factor of $Q = 2000$. Note that these three frequencies represent the broad frequency spectrum present in a *single* impact seismic signal, a feature which will be explored in detail in Section 2.3. As before, we also show the minimum impactor diameter D_p necessary cause the disruption of an asteroid of diameter D_a , using the formulae given in Melosh and Ryan (1997) and Benz and Asphaug (1999). The region bounded by these two sets of curves (shown in gray) indicates that, although reduced as compared to Fig. 2, there remains a broad range of impactor sizes that can produce global seismic effects without disrupting small to medium-sized asteroids. At large target asteroid sizes, however, the impactor size necessary to produce global seismic effects begins to approach the impactor size that can potentially disrupt the body. Consequently, a practical limit for global seismic effects exists, such that asteroids greater than about $\sim 100 \text{ km}$ diameter will experience only localized (regional) seismic effects from individual impacts (although the seismic effects from large impacts will still be widespread over a large portion of the asteroid’s surface). Note also that the lower seismic frequencies suffer less attenuation and therefore penetrate farther than the higher seismic frequencies, a feature observed during the Apollo seismic

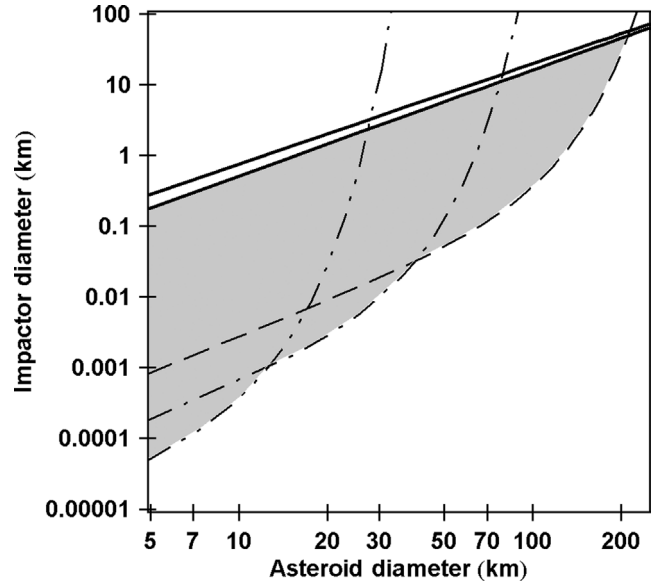


Fig. 7. (Lower curves) Minimum stony impactor diameter necessary to cause $1 g_a$ accelerations throughout the volume of a stony asteroid of given diameter (destabilizing all regolith-covered slopes on the surface), for seismic frequencies f of 1 Hz (dashed), 10 Hz (dot-dashed), and 100 Hz (dot-dot-dashed). In this case, an estimate of seismic attenuation has been included (compare to Fig. 2), such that each seismic frequency has a finite distance over which it will be effective, with lower frequencies penetrating further than higher frequencies. Note that a single impact will produce a seismic frequency spectrum containing all of these frequencies (1–100 Hz). (Upper solid curves) Minimum stony impactor diameter necessary to cause disruption of a stony asteroid of given diameter, calculated per Melosh and Ryan (1997) (top), and Benz and Asphaug (1999) (bottom). The region bounded by these curves, shown in gray, continues to show a wide range of impactor sizes that can cause global seismic effects on small to medium sized asteroids without disrupting them. However, this analytical calculation does point to an upper asteroid size limit of about $\sim 100 \text{ km}$ for global seismic effects from impacts. Larger asteroids will experience localized seismic effects only.

experiments in that the short-period (SP) instruments were only able to detect relatively close impacts (both artificial and meteoritic), while the long-period (LP) instruments were able to detect impacts out to much greater ranges (Dainty et al., 1974; Duennebie and Sutton, 1974; Latham et al., 1968; Toksoz et al., 1974).

2.3. The frequency spectrum of an impact

The goal of the seismic portion of this modeling work is to produce a series of generic, synthetic seismograms typical of impacts on a fractured asteroid. To use the previously derived seismic energy diffusion and attenuation theory to this end (Section 2.1), we first need to find the typical seismic frequency spectrum produced by a small asteroid impact (0.5–500 m impactor diameter). However, with the single exception of Duennebie and Sutton (1974) for lunar impacts recorded via the Apollo 14 short-period (SP) PSE, there are no published power spectra for impact seismic signals. We therefore obtain our power spectra through detailed numerical simulation, using the SALES-2 hydrocode package

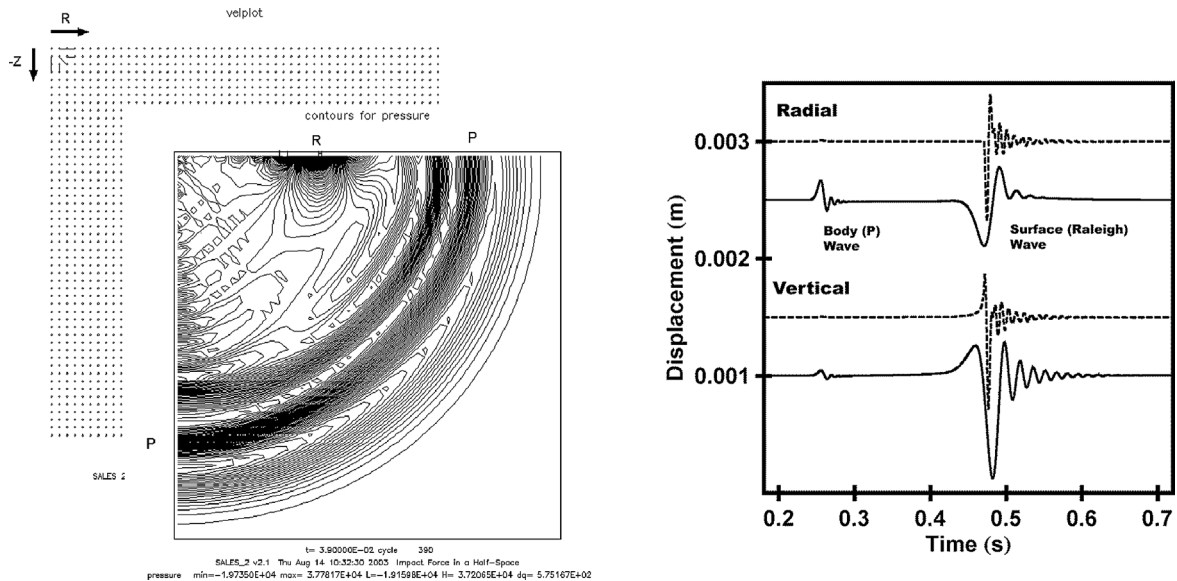


Fig. 8. (Left background) This diagram illustrates the basic components of an impact seismic source, modeled in cylindrical coordinates as part of a hydrocode simulation. Nodal velocity vectors are shown during the initial acceleration of two selected mesh points, one downward and axial ($-z$ direction) and one radial and on the surface (r direction). (Left foreground) The resulting pressure contours in the hydrocode mesh after 0.04 s showing a hemispherical, expanding body (P) wave, and an advancing surface or Rayleigh (R) wave. (Right) Theoretical (*dashed*) and hydrocode produced (*solid*) surface seismograms at 0.5 km distance from an impact into a homogeneous rock half-space, showing a weak body (P) wave arrival at 0.25 s and a strong surface (Rayleigh) wave arrival at 0.5 s. Based on Fig. 2 of Richardson et al. (2004).

(Amsden et al., 1980; Collins et al., 2002) in its most basic mode: monitoring the elastic response of rock to an impact source, without viscosity or accumulated damage (Hooke's law response only).

Rather than modeling an impact directly (with all of its inherent complexity and Lagrangian mesh-stability problems), the impactor is instead treated as an idealized seismic signal source (Lay and Wallace, 1995; Walker and Huebner, 2004), having vertical and radial components in an axially symmetric mesh (left half of Fig. 8). Two individual mesh elements are treated as dynamic point sources, with forces applied to them in the specified component directions. The total amount of energy injected into the mesh is proportional to the impact energy (through the seismic efficiency constant η), while the impulse velocity and duration are consistent with the contact-and-compression phase of a small impact (Melosh, 1989). The motion of the mesh in response to this brief impulse force is then monitored as a function of time to produce synthetic seismograms at various locations on the model's outer free surface, as shown in the right half of Fig. 8 (*solid lines*). We tested this hydrocode seismic modeling method against a theoretical computation of the seismic response of a homogeneous half-space to an impact, using the techniques described in Kanamori and Given (1983) and Richards (1979). The resulting theoretical seismograms compare well with our numerical seismograms (within the frequency resolution limitations of the hydrocode model), and are shown in the right half of Fig. 8 (*dashed lines*).

Asteroids are, of course, not seismically homogeneous bodies, so the numerical modeling was next moved up to

the simulation of an impact into a fractured, multiple material, spherical asteroid—about the size of Dactyl (1-km diameter). Small mesh and cell sizes are required to keep the frequency resolution of the mesh at 125 Hz in the slowest material (used to represent a fault gouge or regolith). This mesh setup is shown in Fig. 9A. The seismic motion of the free surface, shown in Fig. 9B is recorded as a synthetic seismogram, from which the power spectrum is taken.

One important question regarding these hydrocode-produced seismograms is: What is controlling the primary frequencies produced? To answer this question we performed additional (and more typical) hydrocode impact simulations for two different impactor sizes striking both a homogeneous spherical target and a fractured spherical target (as shown in Fig. 9A). Fig. 10 shows the normalized vertical power spectra for a 4- and 60-m impactor striking a 1-km-diameter homogeneous sphere (*left column*) and fractured sphere (*right column*) at 100 m s^{-1} , where the slow speed is necessary to maintain good stability in a Lagrangian mesh for at least 3 s following impact.

These slow-speed simulations indicate that the fracture blocks within the target act as a crude band-pass filter to the injected signal. That is, the fractured body preferentially passes those seismic frequencies close to the harmonic frequencies associated with the mean fracture spacing within the body. Note that even in the case of the larger impactor, which has an inherently lower injected frequency spectrum, the fractured mesh continues to select out the preferred 10–80 Hz range. We therefore choose a fracture structure that produces results consistent with impacts into the upper lunar crust. The resulting seismograms (Fig. 9B) have a frequency

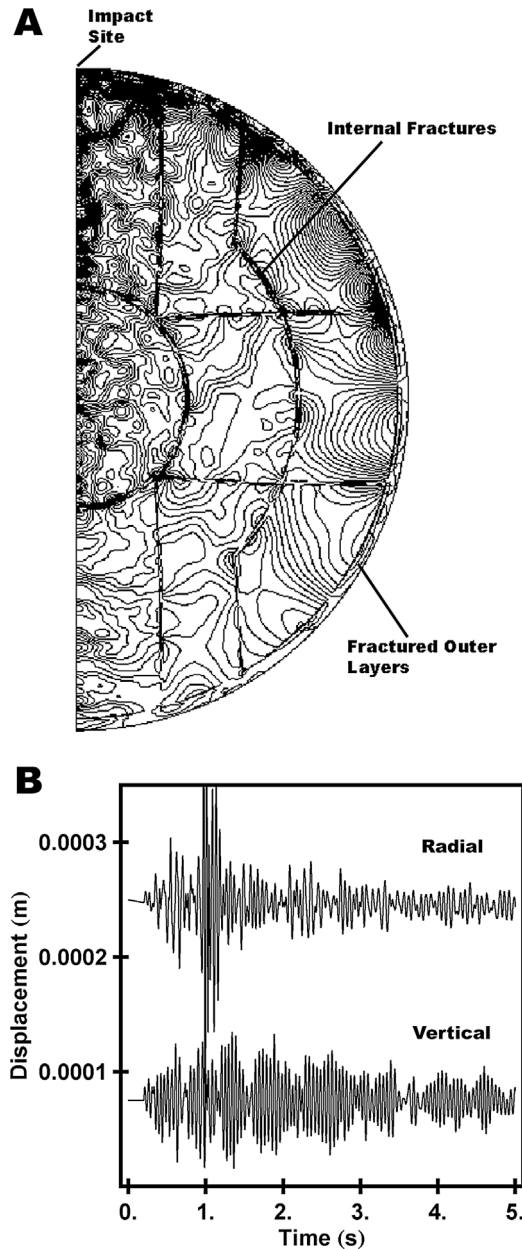


Fig. 9. (A) Cross-sectional view of an axially symmetric hydrocode mesh showing the pressure contours produced by seismic waves propagating through a ‘fractured,’ 1-km-diameter, spherical, rock target following an impact. The wave propagation is a mix of unreflected, reflected, and multiply reflected wave-fronts, such that the propagation of seismic energy is beginning to approach the behavior of a diffusion process. (B) Hydrocode produced surface seismograms at 90° away (half-way around the spherical model surface) from an impact into this ‘fractured,’ 1-km-diameter, spherical, rock target. Note that although the vibrations are extremely mixed in nature, produced by multiple wave-front arrivals (both body and surface waves), an amplitude ‘envelope’ can be discerned in each, particularly in the vertical motion. Based on Fig. 2 of Richardson et al. (2004).

spectrum generally falling between 1 and 100 Hz, with a peak at about 10–20 Hz. Other impact seismic studies have reported peak frequencies of 10–40 Hz (White Sands missile impacts (Latham et al., 1968)), 20–30 Hz (Lunar Active Seismic Experiment (Houston et al., 1973)), and 5–15 Hz

(Lunar Passive Seismic Experiment, short-period instrument (Duennebier and Sutton, 1974)).

With regard to our use of a two-dimensional hydrocode (as compared to a three-dimensional hydrocode), this frequency spectrum matching led us to a fracture spacing of 200–400 m in the mesh, a spacing that would necessarily be smaller in a three-dimensional mesh to achieve the same frequency results. The two-dimensional results, however, are adequate for our purposes since moving to the added complexity of a three-dimensional model would not add significantly to the power and phase spectra obtained. To be consistent with our selected fracture spacing, we additionally adopt a ‘nominal’ mean free path for seismic wave scattering of $l_s = 0.250$ km, although other values will be investigated ($l_s = 0.125$ – 2.000 km).

Also note that free oscillations of the entire, three-dimensional, irregularly shaped asteroid are not important to this study because the frequencies involved with such free oscillations will be out in the low-frequency, low-power ‘wing’ of the frequency spectrum produced by the impact. That is, the oscillation amplitudes necessary to create destabilizing accelerations on the asteroid surface will be long gone by the time the signal decays to the point that whole-body free oscillations dominate.

2.4. Creating synthetic impact seismograms

The diffusion theory for the propagation of seismic energy in a fractured asteroid from Section 2.1 can be combined with the power spectra of an impact seismic signal from Section 2.3 to produce synthetic seismograms for a variety of impactor sizes on a given model asteroid target. To synthesize a generic seismogram for a body having the volume and approximate mean diameter of Eros, we begin by finding the fraction of impactor energy that is converted to seismic energy (using η), and then divide this energy into frequency components in accordance with the power spectra obtained in Section 2.3. Stepping through time, Eq. (10) is then used to simulate the build-up of seismic energy by diffusion and the loss of seismic energy by attenuation for each frequency component. These components are then recombined using inverse Fourier analysis to produce a final seismogram level at each time step.

Fig. 11 shows the typical, ‘far-side’ seismic vibrations resulting from the impact of a 10-m stony object into our Eros-like model asteroid, which would produce an ~ 300 m impact crater on the surface (compare this seismogram to those in Fig. 5). Note that accelerations exceeding the surface gravity of the asteroid (taken to be 5 mm s^{-2}) last for ~ 5 min following the impact. We produced similar generic, synthetic seismograms for a wide range impactor diameters (from 0.5 to 500 m) and our Eros test-case target asteroid. This modeling shows that seismic reverberations exceeding the surface gravity of the asteroid g_a last from a few minutes for impactors of a few meters in diameter, up to about an hour for the largest impactor sizes modeled (a few hundred

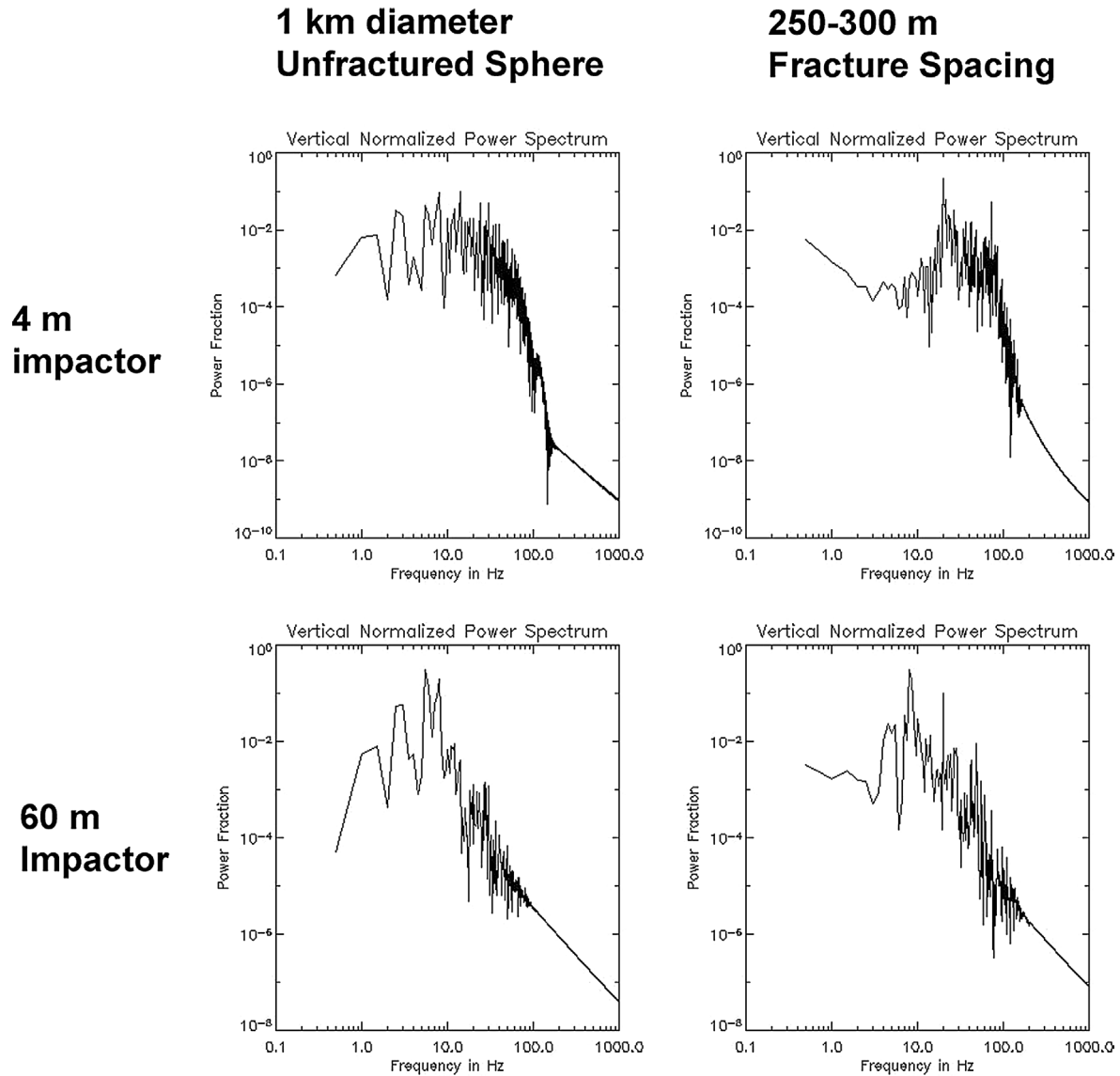


Fig. 10. (Top row) Normalized vertical power spectra (for seismic motion) from a 4-m impactor striking a 1-km-diameter, homogeneous rock sphere (*left*) and fractured rock sphere (*right*) at 100 m s^{-1} . The slow speed helps to maintain stability in a Lagrangian mesh for at least 3 s. (Bottom row) Normalized vertical power spectra (for seismic motion) from a 60-m impactor striking a 1-km-diameter, homogeneous rock sphere (*left*) and fractured rock sphere (*right*) at 100 m s^{-1} . The smaller impactor produces an inherently higher frequency spectrum than that produced by the larger impactor, when no fractures are present. However, when fractures are present these spectra show that the blocks within the fractured mesh act as a crude band-pass filter to the injected signal, preferentially passing those frequencies with wavelengths near the harmonics associated with the typical fracture spacing (about 10–80 Hz).

meters in diameter). The next stage in this study is to investigate how these impact-induced seismic motions will affect the surface morphology of the asteroid. In particular, does this seismic activity cause the degradation of impact craters?

3. Geomorphic modeling

3.1. Downslope motion modeling

To evaluate the effects of seismic shaking on asteroid surface morphology, a downslope motion model was developed which takes the accelerations recorded in the syn-

thetic seismograms described in Section 2.4 and applies them to a hypothetical regolith layer resting on a slope of variable angle, and placed in an asteroid gravity field. For this, we use a form of Newmark slide-block analysis (Newmark, 1965), which can be applied when the regolith layer thickness under consideration is much smaller than the seismic wavelengths involved (Houston et al., 1973; Jibson et al., 1998). This assumption works well for all but the highest impact seismic frequencies, which are the most quickly lost by attenuation. Under this restriction, we can approximate the motion of a mobilized regolith layer by modeling the motion of a rigid block resting on an inclined plane (for discussions of the forces involved, see Lambe

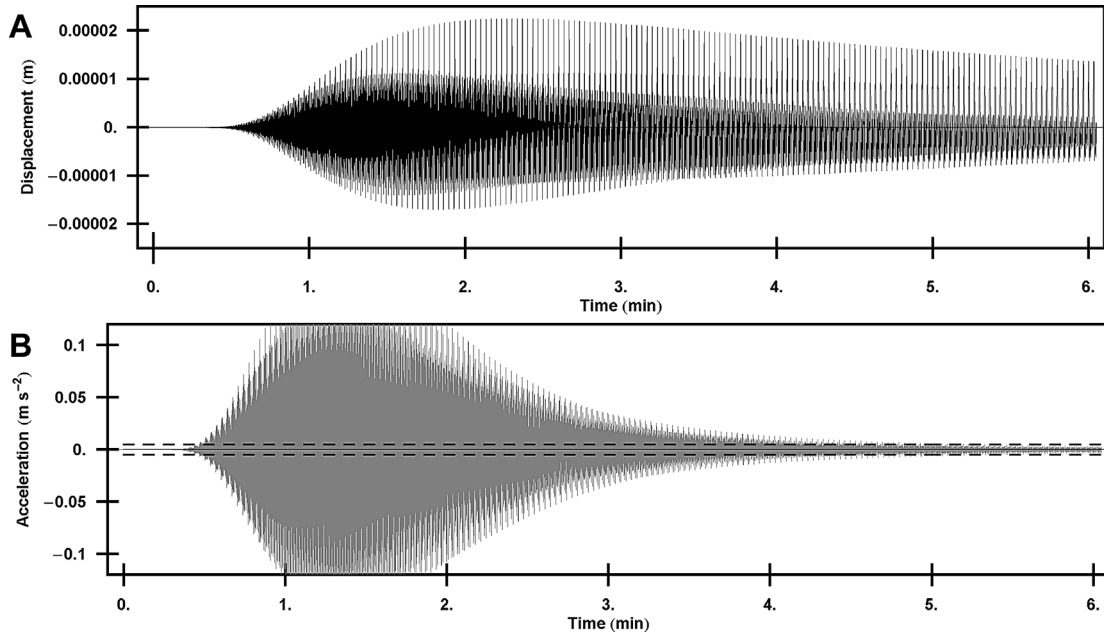


Fig. 11. (A) The first 6 min of a synthetic seismogram for the ‘far-side’ of Eros following the strike of a 10-m stony impactor, showing an asymmetrical, mixed-phase, reverberation signal (compare to Fig. 5). (B) The corresponding seismic accelerations (gray) for the seismogram shown in (A). The two dashed lines indicate the approximate surface gravity magnitude ($g_a = 5 \text{ mm s}^{-2}$), indicating that seismic accelerations that exceed $1 g_a$ last for about 5 min following this impact. Based on Fig. 2 of Richardson et al. (2004).

and Whitman, 1979; Newmark, 1965; Melosh, 1979). We compute the accelerations imparted to the block by the asteroid’s surface gravity (static loading) and seismically shaking slope (dynamic loading) to obtain an overall block (layer) displacement. Fig. 12 shows a schematic view of this model and an example of the type of layer motions achieved during seismic shaking. Note that much of the downslope motion observed is a combination of hopping and sliding, which is much more effective at moving regolith downslope than simple stick-slip motion (horizontal sliding only).

Two types of regolith layers were tested: (1) a Mohr-Coulomb, non-cohesive, uniform porosity, sand-like layer; and (2) a regolith layer having a porosity and cohesion gradient as a function of depth. This second model regolith type stems from the evidence on Eros for weak regolith cohesion (non-zero shear strength), most notably in the form of steep crater walls in small craters which were clearly formed in regolith and ponded deposits (Robinson et al., 2001). On the other hand, broader slope studies indicate that on 300-m scales, only 1–3% of slopes are above typical angles of repose (about 30°), with an observed maximum of 36° (Thomas et al., 2002). Thus, although some features do show indications of cohesion and strength (in the form of crater walls, boulders, outcrops, ridges, and groove edges), areas of obvious regolith coverage all tend to lie below typical angles of repose (Thomas et al., 2002; Robinson et al., 2002). There is also ubiquitous evidence of slope destabilization and the downslope migration of regolith over the entire surface of the asteroid, as mentioned in Section 1.1. This evidence suggests that although present,

existing cohesion forces seem to be relatively easy to overcome.

The importance of even weak cohesive forces in this ‘milli-gravity’ environment can be demonstrated by looking at the Factor of Safety equation for our slide-block model:

$$\text{FOS} = \frac{C + (\mu_s \rho_r g_a h \cos \theta)}{\rho_r g_a h \sin \theta}, \quad (16)$$

where FOS is the factor of safety, C is the cohesion, μ_s is the coefficient of static friction, ρ_r is the regolith density, h is the regolith depth, and θ is the slope angle. Under the gravity conditions on the surface of Eros, a typical dry-sand regolith layer 5 m in depth with a low cohesion value of $C = 100 \text{ Pa}$ can maintain angles of stability (FOS = 1) up to 80° . We therefore felt it necessary to investigate the effects of cohesion in our slide-block modeling. Lacking any actual data on the asteroid’s regolith beyond the evidence provided by the NEAR images, we build a model regolith by (again) relying on the data set collected during the Apollo era on the lunar regolith as our starting point and best analogy.

Analytical calculations of slope factors of safety, angles of stability, and angles of repose indicate that directly applying lunar regolith properties (taken from Houston et al., 1973) in an Eros gravity field results in a regolith layer that can maintain nearly vertical (greater than 85°) slopes up to depths of 20 m. Thus, using the lunar regolith values directly results in a regolith layer which contradicts the visible evidence from Eros, where most regolith slopes lie at below typical values ($<30^\circ$) for the angle of repose (Thomas et al., 2002; Robinson et al., 2002). In an effort to bring the model more in-line with the actual evidence, we therefore

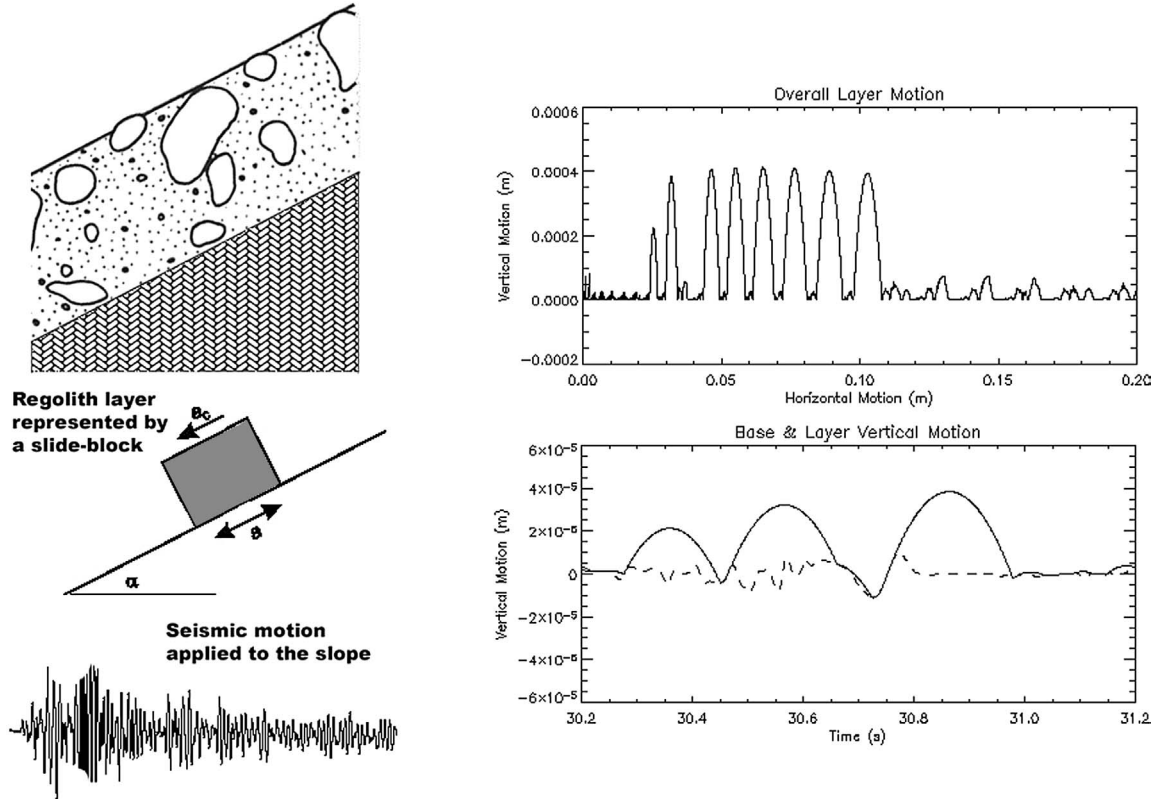


Fig. 12. (Left) A basic illustration of the Newmark slide-block model. The regolith layer resting on a slope is represented by a rigid block resting on an inclined plane. Forces on the rigid block include surface gravity (static loading), seismic accelerations (dynamic loading—applied by the inclined plane), and frictional forces (both static and dynamic). Ballistic launching of the block (layer) is also permitted and tracked in this model. (Upper right) Overall motion of an asteroid regolith layer (1 m depth) resting on a 10° slope, under the seismic shaking conditions produced by a 10-m impactor on the ‘far-side’ of an Eros-like asteroid. Note that the motion involves vertical hopping in addition to horizontal sliding in the asteroid’s very low gravity field ($\sim 5 \text{ mm s}^{-2}$). (Lower right) Close up view of the vertical motion of the inclined plane (*dotted*) and slide-block (*solid*), showing the vertical launching and ‘flight’ of the block (regolith layer) in detail.

reduced the cohesion formula derived for the lunar regolith by an order of magnitude, to obtain the following terms for a hypothetical asteroid regolith:

$$P_r = 0.52 - 0.007h, \quad (17)$$

$$V_r = \frac{P_r}{1 - P_r}, \quad (18)$$

$$C_r = 9.82 \times 10^{(1.14 - V_r)/0.45}, \quad (19)$$

$$\phi_r = \tan^{-1} \frac{0.7}{V_r}, \quad (20)$$

where P_r is the regolith porosity in %, h is the mobilized regolith layer thickness (depth), V_r is the void ratio, C_r is the cohesion in Pascal (N m^{-2}), and ϕ_r is the angle of internal friction.

These formulae give values of regolith cohesion C_r of 13–146 Pa for the first 20 m of regolith depth, which is sufficient to permit angles of stability of $>70^\circ$ for shallow depths (up to a few meters), but also gives angles of repose of $\sim 35^\circ$ – 45° for regolith depths up to 20 m. This large difference between the regolith angle of stability and repose is at least somewhat consistent with the observations described by Robinson et al. (2001), without violating the larger scale regolith properties described by Thomas et al. (2002). Our

hypothetical model regolith is obviously not much more than a guess at the true Eros regolith properties, but does provide us with a way of testing seismic shaking against both a simple non-cohesive regolith and a first-order estimate of a cohesive asteroid regolith.

3.2. Minimum impactor size for global seismic effects (III)

One way of testing our combination of synthetic seismograms and downslope regolith flow modeling is to compare these numerical methods to our previous analytical calculations of the minimum size of impactors necessary to cause global seismic surface effects. Fig. 13 maps out the diameter of impactor necessary to produce greater than $1 g_a$ accelerations (vertical launching) of a $h = 1 \text{ m}$ thick model regolith layer resting on a slight 2° slope, for a variety of asteroid diameters, seismic properties, and the two different regolith types. Fig. 13A uses ‘nominal’ seismic propagation conditions ($\eta = 10^{-4}$, $Q = 2000$) and a non-cohesive regolith layer, while Fig. 13B uses more restrictive seismic propagation conditions ($\eta = 10^{-6}$, $Q = 1000$) and the cohesive regolith model described in Section 3.1. In both cases, a variety of seismic diffusivities K_s values are tested: from

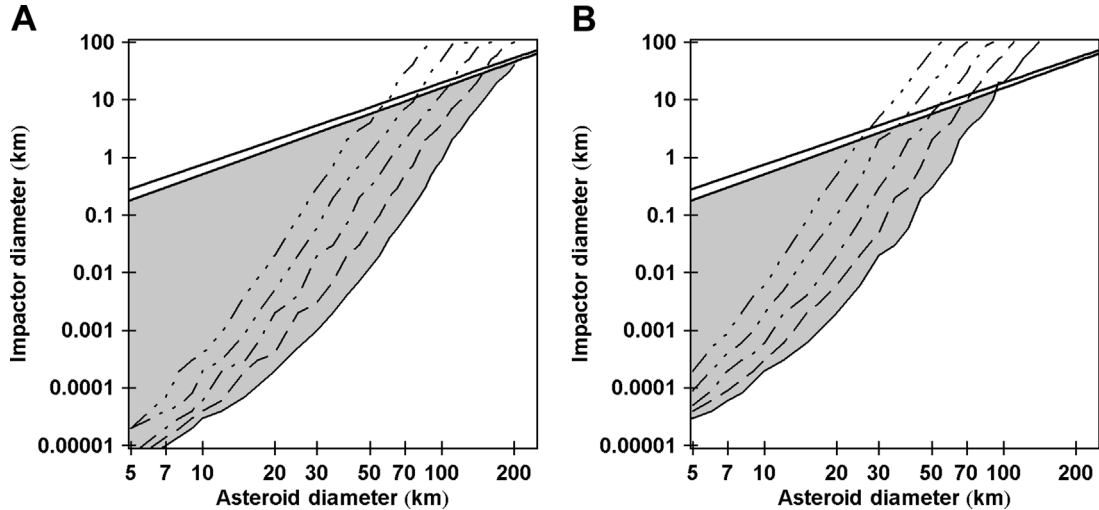


Fig. 13. (Lower curves) A plot of the size of impactor necessary to produce greater than $1 g_a$ accelerations (vertical launching) of an $h = 1$ m thick model regolith layer resting on a slight 2° slope, for a variety of asteroid sizes, seismic properties, and regolith types. For (A) we use ‘nominal’ seismic propagation conditions ($\eta = 10^{-4}$, $v_s = 3 \text{ km s}^{-1}$, $Q = 2000$) and a non-cohesive regolith layer, while for (B) we used more restrictive seismic propagation conditions ($\eta = 10^{-6}$, $v_s = 3 \text{ km s}^{-1}$, $Q = 1000$) and the cohesive regolith model described in Section 3.1. In both cases, a variety of seismic diffusivity values are tested, from $K_s = 0.125 \text{ km}^2 \text{ s}^{-1}$ to $K_s = 2.000 \text{ km}^2 \text{ s}^{-1}$, corresponding to mean free paths for scattering l_s of: 2.000 km (solid), 1.000 km (dashed), 0.500 km (dot-dashed), 0.250 km (dot-dot-dashed), and 0.125 km (dot-dot-dot-dashed). (Upper solid curves) Minimum stony impactor diameter necessary to cause disruption of a stony asteroid of given diameter, calculated per Melosh and Ryan (1997) (top), and Benz and Asphaug (1999) (bottom). The region where global surface effects can occur from a single impact without disrupting the asteroid is shown in gray. This modeling agrees well with our previous analytical calculations (Fig. 7) and indicates an upper asteroid size limit of about 70–100 km for global seismic effects from impacts.

$K_s = 0.125 \text{ km}^2 \text{ s}^{-1}$ to $K_s = 2.000 \text{ km}^2 \text{ s}^{-1}$, corresponding to mean free paths for scattering of $l_s = 0.125\text{--}2.000 \text{ km}$.

This numerical modeling matches the previous analytical result (shown in Fig. 7) quite well and also shows that the mechanism continues to be effective even under the more restrictive conditions used in the second case, Fig. 13B. These results also support a practical limit for impact-induced global seismic effects, such that asteroids greater than about 70–100 km diameter will experience only localized (regional) seismic effects from all but the largest impacts, as previously described in Section 2.2.

With regard to our Eros test case, this slide-block modeling indicates that for an asteroid having the volume and approximate mean diameter of Eros, global downslope motion on all slopes ($2^\circ\text{--}30^\circ$) and for $l_s = 0.250 \text{ km}$ begins at impactor diameters of $\sim 2 \text{ m}$ for a non-cohesive regolith and ‘nominal’ seismic conditions, and $\sim 40 \text{ m}$ for a simple cohesive regolith and more severe seismic propagation conditions. These values are still far smaller than the size of impactor that would disrupt the asteroid, and show the availability of a wide range of impactor sizes capable of triggering the more obvious indications of downslope regolith motion observed on the surface of Eros (shown in Fig. 1).

3.3. Crater degradation by topographic diffusion

The next phase of the study is to demonstrate how seismically triggered downslope flow also contributes to the erosion of cratered topography. We begin by applying our Eros test-case seismograms to a Newmark slide-block model of an $h = 1 \text{ m}$ non-cohesive regolith layer resting on a slope,

done over a wide variety of impactor sizes (0.5–500 m) and slope angles ($2^\circ\text{--}30^\circ$). This modeling yields a set of curves plotting downslope volumetric debris flux per impact q_i ($\text{m}^3 \text{ m}^{-2}$) as a function of slope ∇z (Fig. 14A), which shows one curve for each impactor size. The motion displayed in these curves is typical of non-linear, disturbance-driven downslope regolith transport, and can be described by the equation (Roering et al., 1999):

$$q_i = \frac{K_i \nabla z}{1 - [|\nabla z|/S_c]^2}, \quad (21)$$

where S_c is the critical slope (the slope at which sliding occurs under static loading conditions).

We therefore use Eq. (21) to fit each downslope flux curve and determine the downslope diffusion constant K_i (Fig. 14B solid circles), and the critical slope S_c . Note that under normal sliding conditions, the critical slope S_c would be equal to the coefficient of static friction assigned to the regolith layer in the model, $\mu_s = 0.7$, but due to the ballistic hopping of the layer while in motion, this parameter was better left as a free parameter in the fit, with values of S_c falling between 0.55–0.65 (near the assigned coefficient of dynamic friction, $\mu_r = 0.6$). These fits yield a set of diffusion constants K_i ($\text{m}^3 \text{ m}^{-2}$ per impact) as a function of impactor diameter D_p that follow power-law relationships (see Fig. 14B). These relationships fall into two regimes: $D_p = 1\text{--}4 \text{ m}$, where sliding occurs in stick-slip fashion; and $D_p > 4 \text{ m}$, where sliding occurs in hop-slip fashion. These computed diffusion constant values can be thought of as a ‘maximum’ downslope regolith displacement per impact (on very steep slopes), and as such permit us to perform a rough

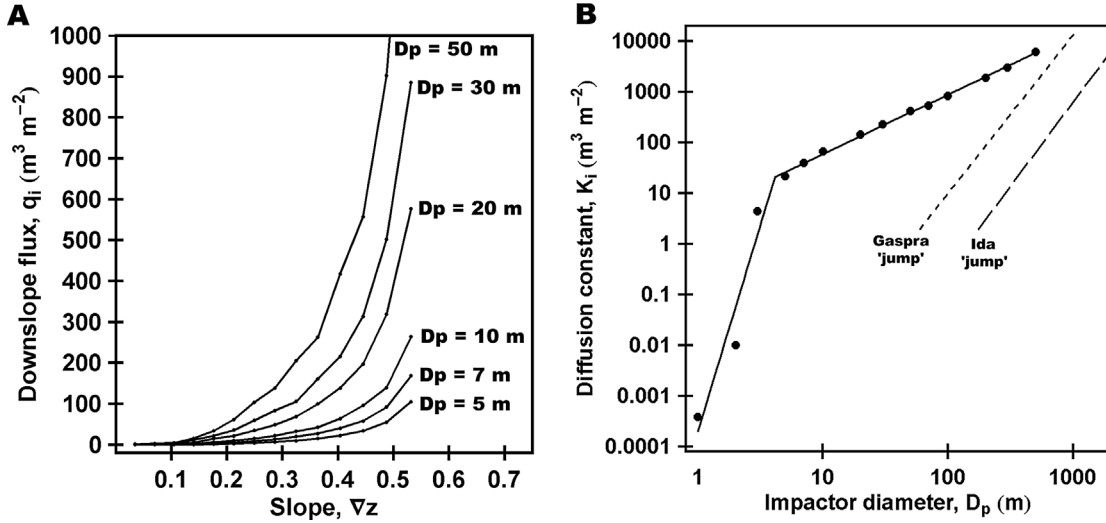


Fig. 14. (A) Newmark slide-block model results for six impactor sizes, plotting volumetric flux per impact q_i ($\text{m}^3 \text{m}^{-2}$) as a function of slope gradient ∇z and displaying the non-linear relationship typical of disturbance-driven flow (Roering et al., 1999). (B) Downslope diffusion constants per impact K_i ($\text{m}^3 \text{m}^{-2}$ or simply m) plotted as a function of impactor size D_p where solid circles show the derived values from Eq. (21) and solid lines shows a linear least-squares fit to these points. The resulting power-law relationships fall into two regimes: $D_p = 1\text{--}4$ m, where sliding occurs in stick-slip fashion; and $D_p > 4$ m, where sliding occurs in hop-slip fashion. This plot is compared with the seismic 'jump' distances reported in Greenberg et al. (1994, 1996), which were estimated from surface velocities on a homogeneous, spherical hydrocode model following impact. Based on Fig. 3 of Richardson et al. (2004).

comparison between these K_i values and the regolith seismic 'jump' distances (per impact) reported in Greenberg et al. (1994, 1996). Shown in Fig. 14B, these ballistic 'jump' distances were estimated from the maximum velocities imparted to the surface of a homogeneous, spherical hydrocode model following impact, and therefore represent the downslope motion resulting from a single seismic 'jolt' (P-wave and Rayleigh wave passage). Not surprisingly, our downslope diffusion constants are significantly greater (by a order of magnitude or more) because in this study we have modeled the amount of downslope motion resulting from the *entire* duration of seismic motion following an impact, which can last from a few minutes to up to an hour.

Note that if the slope ∇z is small, Eq. (21) becomes approximately linear with respect to slope:

$$q_i \approx K_i \nabla z, \quad (22)$$

which will permit the computed values of downslope diffusion per impact K_i to be used in a topographic modification model of the degradation and erasure of impact craters. This modeling is done using an analytical theory of erosion for transport-limited downslope regolith flow first described by Culling (1960). We assume that the downslope flow of regolith is controlled by the transportation rate and not by the regolith supply or production rate (weathering-limited flow) (Nash, 1980). This assumption should hold true for most of the surface of Eros, due to its copious regolith coverage and the ability of impact 'gardening' to produce a continuous supply of loose regolith around each new crater. In this process, classically modeled by Shoemaker et al. (1970) and Gault et al. (1974) for the lunar surface, small impacts overturn a shallow portion of the regolith layer, while larger impacts overturn the regolith at greater depths. Because of

their shallow excavation depths, impacts producing craters up to a few hundred meters in diameter will tend to only 'recycle' the existing regolith (and 'megaregolith') layers, with some small loss of material to space after each impact due to ejection at greater than the escape velocity of the asteroid. 'New' regolith is thus only generated by the largest impacts, which excavate a portion of the fractured bedrock below these regolith layers. It is this constant regolith recycling (with occasional replenishment) that allows us to assume a transport-limited regolith supply.

To develop this erosion theory, we begin with an expression for the conservation of mass on an infinitely small portion of a hillslope, in Cartesian coordinates (Culling, 1960):

$$\frac{\partial z}{\partial t} = - \left[\frac{\partial f_x}{\partial x} + \frac{\partial f_y}{\partial y} \right], \quad (23)$$

where z is the elevation, and f_x and f_y are the flow rates of regolith in the x and y directions, respectively.

If the regolith layer is isotropic with regard to material flow, and the flow rate is linearly proportional to the slope's gradient (as in Eq. (22)), then:

$$f_x = -K_d \frac{\partial z}{\partial x} \quad \text{and} \quad f_y = -K_d \frac{\partial z}{\partial y}, \quad (24)$$

where K_d is a downslope diffusion constant, which has units of $\text{m}^3 \text{m}^{-2} \text{s}^{-1}$ (volume flux per unit time) or m s^{-1} (downslope motion per unit time).

Substituting Eq. (24) into Eq. (23) gives:

$$\frac{\partial z}{\partial t} = K_d \left[\frac{\partial^2 z}{\partial x^2} + \frac{\partial^2 z}{\partial y^2} \right], \quad (25)$$

which we re-write in diffusion equation form:

$$\frac{\partial z}{\partial t} = K_d \nabla^2 z. \quad (26)$$

Because we wish to investigate the degradation of a fresh impact crater due to the infilling of regolith (through downslope flow), we take advantage of the axial-symmetry of the crater's shape and solve this diffusion equation in cylindrical coordinates (r, z). The general solution is given by (based upon the techniques outlined in Kreyszig, 1993):

$$z(r, t) = \sum_{k=0}^{\infty} C_k J_0(kr) e^{-K_d h k^2 t}, \quad (27)$$

where h is the mobilized regolith layer thickness, k is the spatial wave number, and J_0 is a zeroth order Bessel function of the first kind. Note that this equation is a function of time, applicable when the diffusion constant K_d is some constant rate with respect to time (units of either $\text{m}^3 \text{m}^{-2} \text{s}^{-1}$ or m s^{-1}). In our case, however, we have determined a specific amount of downslope diffusion per impact K_i (units of $\text{m}^3 \text{m}^{-2}$ per impact, or simply m per impact), which is itself a function of the impactor's size. Thus, we desire a solution that becomes a function of the number of impacts (and their individual diffusion constants).

Converting to the appropriate variables gives:

$$z(r, t) = \sum_{k=0}^{\infty} C_k J_0(kr) e^{-K h k^2}, \quad (28)$$

where:

$$K = \sum_{i=0}^n K_i, \quad (29)$$

and n is the number of impacts and K_i is the amount of downslope diffusion per impact.

The constant terms, C_k , are computed from the initial topographic form, for which we use a fresh impact crater shape taken from Melosh (1989);

$$C_k = -\frac{dD^2}{128} k^2 D^2 e^{-k^2 D^2 / 16}, \quad (30)$$

where d is the crater depth, D is the crater diameter, and where the crater has an initial d/D ratio of 0.2. Of particular note, the exponential term in Eq. (30) produces a Gaussian distribution of C_k values with a peak amplitude at wave number $k_o = 4/D$.

This solution is used to simulate the degradation (filling) of a crater due to seismic shaking (shown in Fig. 15), given our derived downslope diffusion constants—an effect we call ‘seismic shakedown.’ The most important term in this solution is the relaxation term, $R = e^{-K h k^2}$, and in our modeling the crater is considered to be erased after six $1/e$ decays, $R = e^{-6} = 0.0025$, which gives a depth to diameter (d/D) ratio of 0.0005 when $R = e^{-6}$ is (artificially) assumed over all spatial wave numbers. In actuality, the amount of relaxation for a given amount of downslope regolith diffusion K is strongly dependent upon the wave number k , with higher wave numbers being more strongly affected than lower wave numbers. Thus, sharp crater rims

and other high-frequency features will be the first to relax (erode), while the overall bowl shape of the crater will be the last.

It should also be remembered that the downslope regolith motion displayed in Fig. 14A and described by Eq. (21) is non-linear in nature, such that downslope regolith transport increases significantly with increasing slope. This means that our linearization of the downslope flow (Eq. (22)) makes our degradation model more conservative than what we might actually expect to see on the asteroid surface, with the modeled crater degradation time-scales correspondingly longer. However, our purpose here is to demonstrate the efficacy of the seismic shakedown mechanism, and this first-order, linearized approach serves this purpose well.

Since our Bessel function form of the initial crater shape consists of a narrow Gaussian range of spatial wave numbers, the point at which a crater becomes erased can be approximated by substituting k_o for k in the relaxation term R and equating the arguments $-6 = -K h [4/D]^2$ to give:

$$K \geq \frac{3D^2}{8h}, \quad (31)$$

for the erased state. That is, we find the total amount of downslope diffusion that takes the relaxation term R to e^{-6} for the principle wave number of the crater. When this amount of downslope diffusion K (given by Eq. (31)) is applied to Eq. (28) for all spatial wave numbers, we obtain a depth to diameter (d/D) ratio of 0.0041; at least twice as flat as what could reasonably be detected from NEAR images, $d/D = 0.01$ (Robinson et al., 2002). Equation (31) therefore permits an assessment of an impact crater's ‘seismic damage,’ as downslope diffusion accumulates over time and subsequent impacts (via Eq. (29)) until final crater erasure. This expression will be used in the following section to add the effect of seismic damage to a model of the evolution of the cratering record on the surface of an asteroid.

4. Impact cratering statistics modeling

4.1. A stochastic cratering model

In the final phase of this study, we use these seismic and geomorphic results to model the evolution of the crater size-frequency distribution on a simulated asteroid surface, and show how seismic modification changes the crater population statistics. This model uses Monte Carlo techniques (Press et al., 1992) to populate a two-dimensional continuous test surface, $34 \times 34 \text{ km}$ in size (1156 km^2 , near the Eros value of 1125 km^2 (Robinson et al., 2002)), with craters as a function of time. The simulation then allows these craters to be obliterated by the effects of subsequent impacts: (1) erosion by superposing craters, (2) blanketing by impact ejecta, and (3) erasure by seismic shakedown. The following subsections describe the key components of this model and discuss the results, while the details of the model are described in Appendix A.

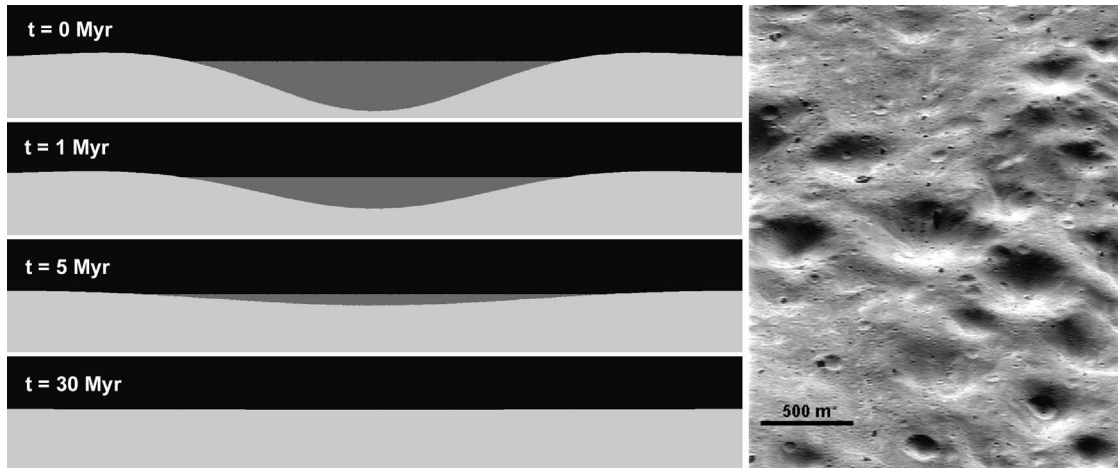


Fig. 15. (Left) Vertical cross-sections taken through a 200-m-diameter crater, shown in *light gray* (horizon level shown in *dark gray*), plotted at four different times and showing its gradual degradation and erasure by impact-induced seismic shakedown on an asteroid having the same volume and surface area as Eros. Complete erasure occurs at a crater age of about 30 Myr in a Main Belt impactor flux. A 20-m crater under the same conditions, will have a life-time of about 300 kyr. Note the rapid initial degradation while the slopes are still relatively high, followed by a more gradual degradation as slopes flatten. (Right) A field of softened and degraded craters on the surface of Eros, showing a range of morphologies consistent with degradation by seismic shakedown (MET 138807458, 154.34 W, 6.15 S, 5.12 m pixel⁻¹).

4.2. The Main Belt impactor population

The impactor population used by this model was selected to represent the average population of asteroids present in the Main Belt, where Eros has spent most of its lifetime (Michel et al., 1998). However, for our modeling purpose, we desired an impactor population in the size range from 0.5 to 500 m, which is below the sizes of asteroid that can be surveyed directly. We therefore have to rely upon model estimates for the distribution of smaller asteroids (impactors) in the Main Belt, from 0.5 to 500 m in size.

The impactor population that we chose for use in our simulations was produced via the asteroid collision and dynamic population modeling performed by O'Brien and Greenberg (2005). O'Brien and Greenberg's asteroid population was derived so as to be consistent with six constraints:

1. the observed population of the Main Belt asteroids from various surveys,
2. the observed population of the near-Earth asteroids from various surveys,
3. the observed number of asteroid families in the Main Belt,
4. the measured cosmic ray exposure ages of meteorites,
5. the preservation of the basaltic crust of Vesta,
6. the observed cratering records on asteroids.

In their model, O'Brien and Greenberg (2005) also includes the Yarkovsky effect as a means of removing small asteroids from the Main Belt and delivering them to the near-Earth population (for a discussion on this effect, see Farinella et al., 1998). Even with this effect added, the cumulative log-log slope of the small Main Belt asteroid population remains relatively steep at ~ -3 , with *no* deficit of small impactors indicated by the model (a deficit suggested

by Chapman et al. (2002) to potentially explain the lack of small craters on Eros).

Fig. 16A shows an expanded view of the numerical distribution of impactor produced by the O'Brien and Greenberg (2005) model, as it compares with similar impactor population models used by Belton et al. (1992) and Greenberg et al. (1994, 1996) to model the cratering records on the Asteroids 951 Gaspra and 243 Ida. In this figure, the vertical axis has been converted from a cumulative number of asteroids to a cumulative number of impacts per year per square kilometer of surface area on the target body, in accordance with the asteroid collision probability estimates described in Bottke and Greenberg (1993).

4.3. Impactor to crater diameter relationship

The relationship between impactor size and resulting crater size on an asteroid-sized body is a subject of continuing study by various researchers. For our modeling, we accept the consensus that crater sizes on these bodies will generally be in the strength-scaling regime at small sizes and transition to the gravity-scaling regime at larger crater sizes, consistent with the numerical hydrocode modeling described in Greenberg et al. (1994, 1996), and Nolan et al. (1996). These studies led us to adopt a simple 'cube-root' scaling-law for Eros such that the resulting crater sizes are directly proportional to the impactor size (Melosh, 1989):

$$D = 30D_p. \quad (32)$$

This scaling-law is plotted in Fig. 16B, showing it in comparison to strength scaling (Holsapple, 1993), gravity scaling (Holsapple, 1993; Melosh, 1989), and the hydrocode simulations for 951 Gaspra and 243 Ida (Greenberg et al., 1994, 1996).

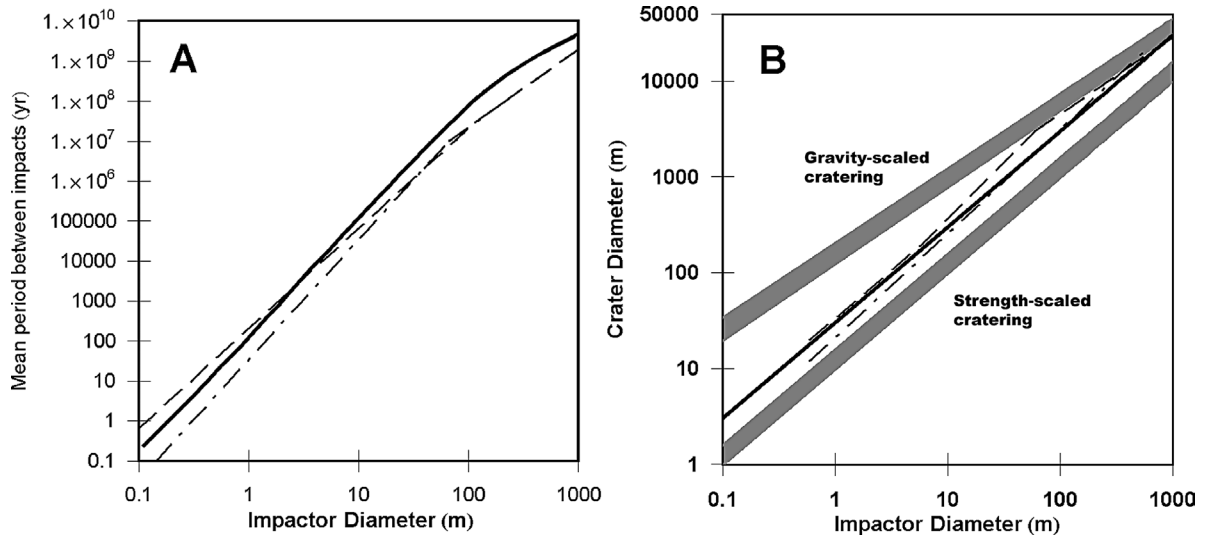


Fig. 16. (A) An inverted cumulative distribution curve showing the mean time between impacts from impactors of a given size (or greater) on a spherical asteroid with a surface area matching that of 433 Eros (1125 km^2). In this work we use an impactor population produced by the modeling described in O'Brien and Greenberg (2005) (solid), which has a cumulative log–log slope of 2.93 for impactor diameters D_p in the range $0.1 < D_p < 95 \text{ m}$, and shallowing to a cumulative log–log slope of ~ 1 for impactor diameters $D_p > 95 \text{ m}$. Also plotted are the similar impactor populations used by Belton et al. (1992) (dashed) and Greenberg et al. (1994, 1996) (dotted) to model the cratering records on the Asteroids 951 Gaspra and 243 Ida. (B) A plot of the simple $30\times$ scaling-law used in this study for mapping impactor size to crater size (solid), showing it in comparison to strength scaling (Holsapple, 1993), gravity scaling (Holsapple, 1993; Melosh, 1989), and the hydrocode simulations for 951 Gaspra (dot-dashed) from Greenberg et al. (1994) and 243 Ida (dashed) from Greenberg et al. (1996). The gray bands represent a variety of target material types, from loose sand to competent rock. Note that the size of impactors used in our stochastic cratering model range from 0.667 m (producing 20 m craters) to 667 m (producing 20 km craters).

4.4. The 433 Eros cratering record

Equipped with a workable model for the evolution of craters on the surface of an asteroid, we next attempt to recreate the statistics of the cratering record on the surface of 433 Eros, included the observed paucity of small craters. Example screens from this stochastic cratering model are shown in Fig. 17, which display model runs *without* and *with* (respectively) the effects of seismic shakedown included. A relative size-frequency distribution plot (R-plot) of the model output is also shown in Fig. 18 for the case which includes the effects of seismic shakedown (Arvidson et al., 1979). In both figures, the observed (Chapman et al., 2002; Robinson et al., 2002) and modeled distributions are in good agreement (for craters $> 100 \text{ m}$) at a Main Belt exposure age of $400 \pm 200 \text{ Myr}$. Note that this age is neither an absolute age for Eros, since major impacts can potentially 'reset' the asteroid surface record (Greenberg et al., 1994, 1996), nor is it an accurate age for the current surface record, because the chaotic nature of Eros's orbit has exposed it to a highly variable impactor flux (Michel et al., 1998)—rather than the assumed constant flux used in our modeling. At best, this surface age represents a lower limit, assuming that an average Main Belt impactor flux is at the high end of what Eros has actually been exposed to. The observed and modeled crater populations differ at larger crater sizes ($> 2 \text{ km}$), where the statistics of small numbers and random crater generation make matching the observed crater population at this end of the curve difficult. The simulations lead to two possibilities to explain this mismatch:

1. the age obtained could be an absolute Main Belt exposure age for Eros, and we have simply not had a model run which generates the correct large crater population to match the observed distribution, or
2. the number of very large craters on Eros is indicative of a much older body than the current cratering record reflects, such that the measured Main Belt exposure age reflects the time elapsed since the last major impact event, which 'reset' the small crater record (Greenberg et al., 1994, 1996).

Additional modeling tends to support the latter interpretation, in that good matches to the large crater record ($> 2 \text{ km}$) are obtained after about 1–2 Gyr. At these model ages, however, the 'dip' in the Eros cratering record between 1 and 6 km diameters is replaced by standard 'empirical saturation' levels, since the current model does not simulate global cratering record resets from very large impact events.

Note that it is only in Figs. 17B and 18—where the effects of seismic shakedown are included—that the observed small cratering record is matched by the models. The reduced number of small craters is a result of seismic erasure (cumulative seismic damage via Eqs. (29) and (31)), causing lower equilibrium crater numbers for craters $< 100 \text{ m}$ diameter than would otherwise be expected (empirical saturation). This equilibrium point is a sensitive function of the assumed thickness of the mobilized regolith layer h . By varying this parameter, we find a best fit corresponding to $h \approx 0.1 \text{ m}$, with actual values for h perhaps as high as a few meters (due to the assumptions and uncertainties in our

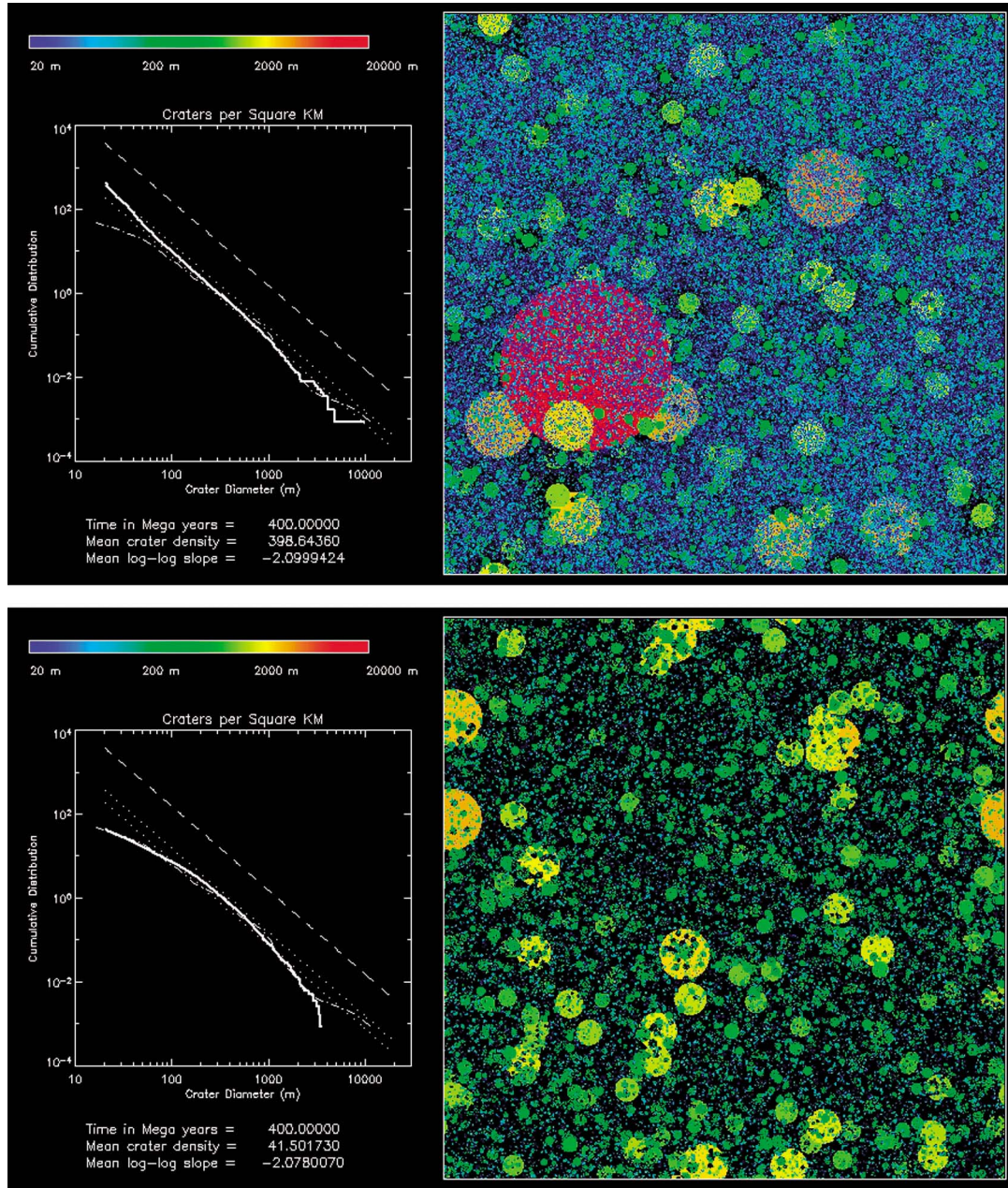


Fig. 17. Example screens from the stochastic cratering model following 400 Myr of impacts on an Eros-like target body. The area shown in these displays is 34×34 km (1156 km^2), with a model resolution of 20×20 m. Craters are color coded by size (see color bar). The curves shown in the cumulative distribution plots are: geometric saturation (*dashed*), estimates of empirical saturation at 5–10% geometric saturation (*dotted*), modeled crater distribution (*thick solid*), and the observed crater distribution on 433 Eros (*dot-dashed*) from Chapman et al. (2002); Robinson et al. (2002). (Top) Crater population after 400 Myr *without* seismic shaking included in the simulation. Note the empirical saturation level of small craters and a poor match with the observed distribution of craters on Eros. (Bottom) Crater population after 400 Myr *with* seismic shaking included in the simulation. Note the excellent match between the modeled and observed crater distributions, particular with regard to small craters (less than 100 m diameters).

modeling). This value is significantly less than the estimates for a loose regolith layer thickness on the order of ‘tens of meters’ from the NEAR observations (Thomas et al., 2002; Robinson et al., 2002). We infer from this difference that much of the regolith layer possesses a depth-dependent porosity and cohesion gradient, perhaps due to compaction from seismic shaking. This characteristic would produce lower porosity and higher cohesion with increasing depth (Robinson et al., 2002). Such a gradient was observed for

the lunar regolith (down to sampling depths of a few meters), and would cause the regolith layer to preferentially slide (or ‘break’) at shallow critical depths, rather than mobilizing the entire regolith layer (Houston et al., 1973).

It should be pointed out that based upon this study, large asteroids greater than about 70–100 km diameter (see Figs. 7 and 13) should not experience the same degree of small crater erasure as asteroids in the size range of Eros, and should therefore have small crater equilibrium numbers ap-

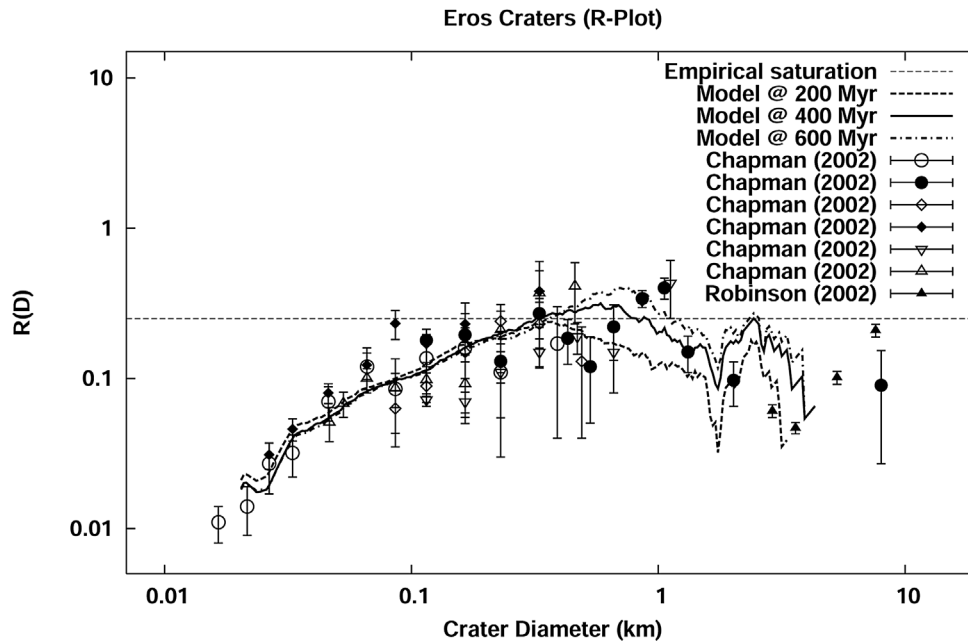


Fig. 18. A relative size-frequency distribution plot (Arvidson et al., 1979) of 433 Eros craters per square kilometer as a function of crater diameter, showing a favorable comparison between observed (Chapman et al., 2002; Robinson et al., 2002) and modeled values after 400 ± 200 Myr (Main Belt exposure age). The low abundance of small craters is a result of seismic erasure, causing lower equilibrium values than would otherwise be expected (empirical saturation; thin dashed line). Symbols are the same as those listed in Table 1 of Chapman et al. (2002). Based on Fig. 4 of Richardson et al. (2004).

proaching more typical ‘empirical saturation’ levels (the dotted lines in Fig. 17). Such bodies should only experience localized seismic effects from all but the largest impacts, and not the global seismic effects modeled in this study. As an example of a much larger body, the Earth’s moon does show some minor, local variations in small crater numbers depending upon the surface material and age; however, most areas display rather typical levels of empirical saturation at small crater diameters (5–200 m) when observation effects, such as sun angle, are taken into account (Schultz et al., 1977).

4.5. The enigma of ponded deposits on Eros

One of the most extraordinary finds of the NEAR–Shoemaker mission was the ponded deposits found in small craters up to a few hundred meters in diameter (see Fig. 19). These ponds show clear evidence of downslope material motion, and impact-induced seismic shaking has been suggested as a possible means for their formation (Cheng et al., 2002b). However, the ponds display several features, described in Robinson et al. (2001), that differ from the model of downslope motion and crater erosion that we have established in this work:

- A difference in geomorphology: the ponds appear as extremely flat deposits in the bottoms of craters and topographic lows, while craters degraded by seismic shake-down maintain their curving, bowl shape and slowly ‘soften’ over time (Fig. 15).
- An apparent difference in flow style: the very flat ponded deposits are indicative of a frictionless, fluid-

like flow, while the downslope flow induced by seismic shaking involves frictional forces and requires a slope (gradient) to occur (Section 3.3).

- A difference in localities: the ponded deposits are concentrated primarily in areas of prolonged terminator exposure and low surface gravity, while impact-induced seismic effects should be global in distribution.
- A difference in grain-size: the ponds appear visually to be composed of finer-grained material than their surroundings, a conclusion supported by their bluer color, while debris flow induced by seismic shaking would tend to be more assorted (or even cause the *larger* grain sizes to rise to the top via the ‘Brazil Nut’ effect (Asphaug et al., 2001)).

These features all lend support to electrostatic dust levitation (Lee, 1996; Colwell et al., 2005) as the mechanism for the formation of ponded deposits on Eros, as originally suggested in Robinson et al. (2001). There may be areas where the two effects are mixed, with seismic shaking acting as the bulk mover of material downslope and the primary agent of crater erosion, but with electrostatic dust levitation producing a veneer of thin, flat deposits during the time periods between major impacts. This mixing of two different processes is supported by the presence of morphologically ‘fresh’ ponds located in the bottom of heavily degraded (softened) craters (Robinson et al., 2002). It is possible that while Eros was located in the Main Asteroid Belt, seismic shaking was the dominant force for downslope flow and surface modification. However, now that Eros has moved to the

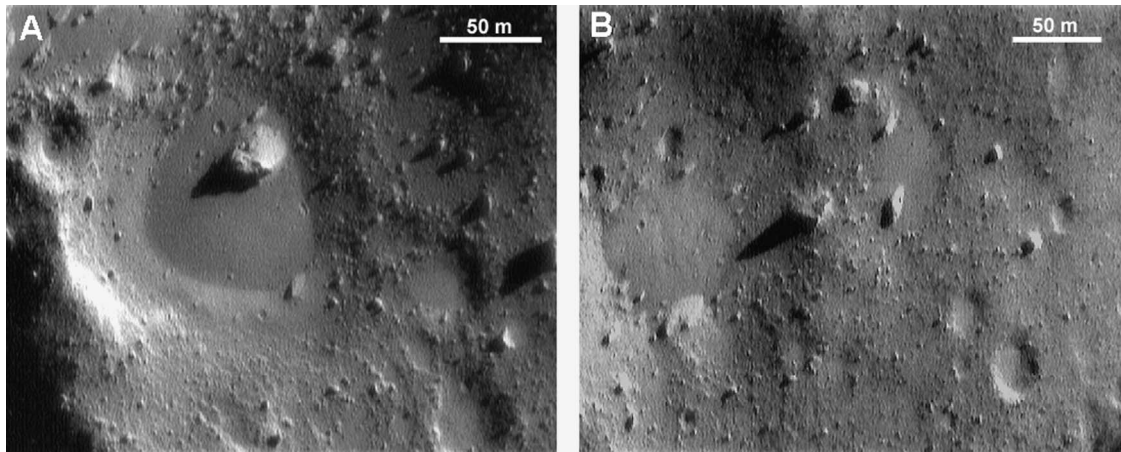


Fig. 19. Two examples of ponded deposits on 433 Eros, imaged by the NEAR–Shoemaker spacecraft. Note the marked difference in morphology between these ponds and the degraded craters shown Fig. 1 (D) and Fig. 15, indicative of different formation processes. The ponds shown here are located on the low surface-gravity ($2.5\text{--}3.0\text{ mm s}^{-2}$) ‘nose’ of the asteroid, which also spends a longer than average amount of time near the terminator (light/dark boundary). (A) A beautiful 100-m diameter ponded deposit containing an embedded 25 m boulder. Note the extremely flat surface containing a tiny (few-meter diameter) impact crater (MET 155888598, 179.04° W , 2.42° S , 0.55 m pixel^{-1}). (B) A smaller 75-m diameter ponded deposit. Note the difference between the smooth, fine-grained pond surface and the coarse, boulder strewn terrain surrounding the deposit (MET 155888731, 183.88° W , 3.21° S , 0.63 m pixel^{-1}).

near-Earth asteroid environment, the impactor flux has been reduced by a factor of $10^2\text{--}10^3$ (Ivanov et al., 2002) and the solar flux has increased by factor of about 4. Thus electrostatic dust levitation could currently be the dominant surface modification mechanism on the asteroid. At the least, the much longer (on average) intervening time period between major impacts permit electrostatically formed ponds to form and grow to larger sizes than previously, without seismic disruption.

The suggestion has also been made that electrostatic dust levitation may be the cause for the deficit in small crater numbers on 433 Eros (Asphaug, 2004), rather than seismic shakedown. However, the paucity of small craters on Eros has a *global* distribution, as does the distribution of degraded and softened craters (Chapman et al., 2002; Robinson et al., 2002), while ponded deposits are concentrated primarily in areas of prolonged terminator exposure and low surface gravity, and therefore have very localized distributions (Robinson et al., 2001). Additionally, if ponded deposits were the agent of small crater erasure, we should have observed a wide variety of crater-pond ‘fill’ levels, covering the full range from light veneers in the bottom of fresh craters to nearly flat, circular depressions (almost filled craters). Instead, the observed ponded deposits filled only a small fraction of the bowls of those craters which had ponds, with a maximum depth of just a few meters in the largest craters (Robinson et al., 2001, 2002). Further analysis showed that very little material ($<0.2\text{ m}$) needs to be removed from the interior slopes of a host crater to form a pond, assuming no exterior source for the deposit (Robinson et al., 2002). This evidence suggests strongly that although an important surface modification mechanism, pond formation (most likely from electrostatic dust levitation) is *not* the mechanism for small crater erasure on the asteroid.

5. Conclusion

For 433 Eros, the modeling work presented here has produced excellent agreement with the empirical observations, particularly with regard to the time evolution of crater morphology and the statistics of the impact cratering record. Nevertheless, we note that there is considerable uncertainty with regard to the asteroid’s actual seismic and regolith properties. We have based our results on values appropriate to the one impact-generated environment that has been studied in detail: the upper lunar crust. Even with these uncertainties, however, this work constrains these properties and effectively demonstrates the ability of impact-induced seismic shaking of an Eros-sized asteroid to destabilize slopes, cause regolith to migrate downslope, and to degrade and eventually erase small impact craters on the surface. Additionally, this result lends support to an internal ‘fractured monolith’ structure for Eros, and also supports asteroid population models that produce a steep population of small asteroids despite removal by the Yarkovsky effect.

While the true efficacy of this mechanism (and the accuracy of our modeling) will not be shown until seismometers are landed on asteroid surfaces and their response to artificial and natural impacts measured, an earlier test of this work will occur when detailed images of large Main Belt asteroids (greater than 70–100 km diameter) are returned. Such asteroids should exhibit less small-crater erasure, due to the lack of global seismic effects, and should therefore have small crater numbers more indicative of the actual small impactor population (or show more typical empirical saturation levels).

This modeling also demonstrates the potential of seismic studies of asteroids to investigate their interiors. Such studies could not only give us information about the internal structure of these bodies; such as major fracture boundaries, inter-

nal stratigraphy, voids, and small-scale fracture spacing; but could also provide information about the rock composition, compositional variations, elastic response, and seismic dissipation properties. Both reflection and standard seismological techniques could be employed, building upon our experience with the Apollo seismic experiments and taking advantage of the advances that have occurred in the field since that time. We look forward to the openings that this tool offers toward our understanding of these fascinating objects.

Acknowledgments

The authors thank Hiroo Kanamori (California Institute of Technology) for the use of his theoretical seismic code for Lamb pulse seismic sources, Clark Chapman (Southwest Research Institute) for the use of his crater count data for Eros, and Virginia Smith (Lunar and Planetary Laboratory) for illustrating assistance. This research is supported by Grant NAG5-12619 of NASA's NEAR Data Analysis Program and NAG5-11493 of NASA's Planetary Geology and Geophysics Program.

Appendix A. Stochastic cratering model

A.1. Basics of the Monte Carlo cratering model

As described in Section 4, the stochastic cratering model uses Monte Carlo techniques (Press et al., 1992) to populate a model surface with craters as a function of time and then allows them to be eroding by superposing craters, covered with impact ejecta, and seismically shaken by subsequent impacts. The model is loosely based upon similar, previous models (Woronow, 1978; Chapman and McKinnon, 1986) and consists of six two-dimensional matrix layers (representing the surface area of an asteroid) to form a 'pseudo three-dimensional' model. Two layers are used to store crater diameter values, two are used to store ejecta coverage values, and two are used to store crater seismic damage values. The purpose for having two sets of information is to permit the superposition of smaller craters on top of larger craters, while preserving the information about the larger crater (below). The superposing and other crater erasure rules are explained in the following sections.

The computer program begins by setting up a blank asteroid surface area for study, consisting of a six-layer 1700×1700 element matrix, where each element represents a 20×20 m pixel⁻¹ on a 34×34 km surface area (1156 km², close to the Eros surface area of 1125 km² (Robinson et al., 2002)). All six matrix layers (crater diameters, ejecta coverage, and seismic damage) begin at zero values. The program next reads in a supplied data file which gives the probability of an impact from a particular sized impactor per year per square kilometer on the surface of an asteroid in the Main Belt, based on the population derived by O'Brien and

Greenberg (2005). It then uses a random number generator and the supplied probabilities to produce a series of random impactor sizes and impact locations on the surface. Crater diameters are calculated from the impactor size, and each new crater is placed on the surface by writing the crater's diameter value to all pixel elements within the crater's radius, in accordance with the superposition rules described below. Also, within the new crater's radius, all ejecta coverage and seismic damage values are set to zero. Note that the model matrix has periodic boundary conditions, such that craters positioned near a border (either vertical or horizontal) are wrapped around to the opposite side of the matrix. In effect, this creates a smooth, continuous surface area for study, without boundaries and boundary effects on the crater counting.

A.2. Erasure by crater superposing

Two matrix layers are maintained to store the crater diameter values: a 'first generation' layer and a 'second generation' layer. The first generation layer is generally the more permanent layer, storing information about larger and longer lasting craters. The second generation surface is generally the more temporary layer, particularly for small craters superposed upon a larger crater but not contributing to the erasure of the larger crater. Initially, new craters are written onto both 1st and 2nd generation layers, until superposing begins to occur. In that case, the program decides whether a new crater actually erases a portion of an older, pre-existing crater (1st generation) or is just superposed upon the surface of the older crater (2nd generation) with the older crater intact underneath. In order to erase a portion of a larger pre-existing crater, the new crater must have a diameter which is at least 1/10 the diameter of the pre-existing crater (Soderblom, 1970). If erasure or writing to a blank surface occurs, then the new crater is written onto both 1st and 2nd generation layers, while if a superposition only occurs, then the new crater is written only onto the 2nd generation layer. If a 2nd generation crater is subsequently erased by ejecta or seismic shaking later, it is 'cleaned off' the 2nd generation layer and any pre-existing 1st generation crater underneath is restored to the master 2nd generation layer above. All of these events occur on an element by element basis, such that once a crater is implanted, it is treated only in a unit area fashion from that moment on, not as an entire feature.

This erasure and superposition method is based upon the principle of impact gardening (see Melosh, 1989, for details) and the crater erosion work described in Soderblom, 1970, in which each new crater will only affect and turn over a depth of rock and regolith which is about 1/8–1/12 of its diameter. For example, while new, very small craters (tens of meters in diameters) can superpose themselves on the larger craters on Eros, such as Himeros (~10-km diameter), Shoemaker (7.6-km diameter), and Psyche (5.3-km diameter), they cannot erase these features—it takes a new impact on the same size scale as the old one to actually erase a portion of it, such

as the portion of Himeros which has been removed by the emplacement of Shoemaker.

A.3. Erasure by crater ejecta coverage

Whenever a new crater is formed (whether 1st generation or 2nd generation), the area within 5 crater radii of the impact site is affected by and examined for possible crater erasure by the ejecta blanket emplaced by the new impact. The ejecta blanket thickness (height) as a function of distance from the new crater center is found using Eq. (6.3.2) from [Melosh \(1989\)](#):

$$H_b = 0.14R^{0.74} \left[\frac{r}{R} \right]^{-3}, \quad (\text{A.1})$$

where H_b is the ejecta blanket thickness, r is the distance from the crater center, and R is the new crater radius. Note that this equation is based upon lunar craters, and will therefore require an upgrade as additional work is done on asteroid craters and ejecta. It also assumes gravity dominated cratering only—a problematic assumption on its own, especially near the small crater end of the asteroid cratering scale.

If we assume that a crater is parabolic in shape and has a d/D ratio of $1/5$, then the crater volume V and area A are given by:

$$V = \frac{1}{40} \pi D^3, \quad (\text{A.2})$$

$$A = \frac{1}{4} \pi D^2. \quad (\text{A.3})$$

Dividing V by A implies that if the area of the crater A is covered by ejecta to a depth of $1/10 D$, the crater should be effectively filled (perhaps with agitation by seismic shaking from subsequent impacts). Two matrices (one for 1st generation and one for 2nd generation craters) keep track of the total amount of ejecta collected per unit surface area (crater element) in each crater, and when the depth in a given mesh element reaches $1/10 D$ of the crater in question, that unit area is considered filled or erased.

This ejecta erasure method is admittedly rather simplistic, but adding to the sophistication of the method with our current knowledge level regarding ejecta blanketing on small bodies is unwarranted. As this gap is filled in, a more complicated method can be incorporated.

A.4. Erasure by seismic shaking

Two separate matrix layers are used to track seismic damage to both 1st generation and 2nd generation craters. If a new crater's impactor is at least 1 m in diameter, then all other craters on the 1st and 2nd generation surfaces receive seismic damage in accordance with Eq. (29); that is, a value of downslope diffusion K_i is computed for each new impact, and this value is added to the total diffusion sum K for all mesh elements outside of the new crater's radius. If the total diffusion sum K for a particular crater element equals or

exceeds the value computed by the right side of Eq. (31) for that crater, then that unit area is considered filled or erased.

A.5. Observation rules

Because the craters produced by this model are handled in a per-unit-area (pixel) fashion during crater production and erasure, some rules need to be applied when they are counted for the production of a crater size-frequency distribution curve. Actual crater counting requires that at least enough of the rim of the crater remains, such that a radius of curvature can be estimated within the resolution limits of the image being examined. To incorporate a semblance of this feature of crater counting into this model, We use simple rules specifying that some fraction of the original crater area must remain in order to be counted. These rules are currently that $>25\%$ of craters >200 m in diameter must remain to be counted, $>50\%$ of craters between 130 and 200 m must remain to be counted, $>75\%$ of craters between 100 and 130 m must remain to be counted, and that 100% of craters <100 m must remain to be counted. Note that these rules are heavily affected by the pixelation of the craters, especially for craters less than 100 m (5 pixels across). These observation rules were derived practically by calibrating the model at empirical crater saturation levels (without seismic shaking) to produce a relatively straight log–log cumulative distribution at about 7–8% of geometric saturation (for discussion see [Melosh, 1989](#)).

A.6. Global cratering record resets?

At the large end of the impactor scale, the vertical velocities imparted to the rigid block in the Newmark slide-block model begin to approach the escape velocity of the asteroid. In these instances, it is assumed that the Newmark model begins to break down, and that a global upset and re-arrangement of the asteroid's regolith (and some underlying fractured bedrock) will occur. This effect was estimated in [Greenberg et al. \(1994\)](#) and then used to explain the unusual shape of the size-frequency distribution of craters on 951 Gaspra. This effect requires further investigation, and has not yet been implemented in the impact cratering model.

References

- Amsden, A.A., Ruppel, H.M., Hirt, C.W., 1980. Sale: A simplified ALE computer program for fluid flows at all speeds. LA-8095 Report, Tech. Rep. Los Alamos National Laboratories, Los Alamos.
- Arvidson, R.E., Boyce, J., Chapman, C., Cintala, M., Fulchignoni, M., Moore, H., Neukum, G., Schultz, P., Soderblom, L., Strom, R., Woronow, A., Young, R., 1979. Standard techniques for presentation and analysis of crater size-frequency data. *Icarus* 37, 467–474.
- Asphaug, E., 2004. Nothing simple about asteroids. *Science* 306, 1489–1492.
- Asphaug, E., Melosh, H.J., 1993. The Stickney impact of Phobos—A dynamical mode. *Icarus* 101, 144–164.

- Asphaug, E., Moore, J.M., Morrison, D., Benz, W., Nolan, M.C., Sullivan, R.J., 1996. Mechanical and geological effects of impact cratering on Ida. *Icarus* 120, 158–184.
- Asphaug, E., King, P.J., Swift, M.R., Merrifield, M.R., 2001. Brazil nuts on Eros: Size-sorting of asteroid regolith. *Lunar Planet. Sci. XXXII*. Abstract 1708.
- Belton, M.J.S., Chapman, C.R., Klaasen, K.P., Harch, A.P., Thomas, P.C., Veverka, J., McEwen, A.S., Pappalardo, R.T., 1996. Galileo's encounter with 243 Ida: An overview of the imaging experiment. *Icarus* 120, 1–19.
- Belton, M.J.S., Veverka, J., Thomas, P., Helfenstein, P., Simonelli, D., Chapman, C., Davies, M.E., Greeley, R., Greenberg, R., Head, J., 1992. Galileo encounter with 951 Gaspra—First pictures of an asteroid. *Science* 257, 1647–1652.
- Benz, W., Asphaug, E., 1999. Catastrophic disruptions revisited. *Icarus* 142, 5–20.
- Botke, W.F., Greenberg, R., 1993. Asteroidal collision probabilities. *Geophys. Res. Lett.* 20, 879–881.
- Botke, W.F., Nolan, M.C., Greenberg, R., Kolvoord, R.A., 1994. Velocity distributions among colliding asteroids. *Icarus* 107, 255–268.
- Britt, D.T., Yeomans, D., Housen, K., Consolmagno, G., 2002. Asteroid density, porosity, and structure. In: Botke Jr., W.F., Cellino, A., Paolicchi, P., Binzel, R.P. (Eds.), *Asteroids III*. Univ. of Arizona Press, Tucson, pp. 485–500.
- Carr, M.H., Kirk, R.L., McEwen, A., Veverka, J., Thomas, P., Head, J.W., Murchie, S., 1994. The geology of Gaspra. *Icarus* 107, 61–71.
- Carslow, H.S., Jaeger, J.C., 1959. *Conduction of Heat in Solids*, second ed. Oxford Univ. Press, Oxford.
- Chapman, C.R., 1978. Asteroid collisions, craters, regoliths, and lifetimes. In: *Asteroids: An Exploration Assessment*. NASA, Washington, pp. 145–160.
- Chapman, C.R., McKinnon, W.B., 1986. Cratering of planetary satellites. In: *IAU Colloq. 77: Some Background about Satellites*, pp. 492–580.
- Chapman, C.R., Merline, W.J., Thomas, P.C., Joseph, J., Cheng, A.F., Izenberg, N., 2002. Impact history of Eros: Craters and boulders. *Icarus* 155, 104–118.
- Cheng, A.F., Barnouin-Jha, O., Prockter, L., Zuber, M.T., Neumann, G., Smith, D.E., Garvin, J., Robinson, M., Veverka, J., Thomas, P., 2002a. Small-scale topography of 433 Eros from laser altimetry and imaging. *Icarus* 155, 51–74.
- Cheng, A.F., Izenberg, N., Chapman, C.R., Zuber, M.T., 2002b. Ponded deposits on Asteroid 433 Eros. *Meteor. Planet. Sci.* 37, 1095–1105.
- Cintala, M.J., Head, J.W., Veverka, J., 1978. Characteristics of the cratering process on small satellites and asteroids. *Proc. Lunar Sci. Conf.* 9, 3803–3830.
- Collins, G.S., Melosh, H.J., Morgan, J., Warner, M.R., 2002. Hydrocode simulations of Chicxulub crater collapse and peak-ring formation. *Icarus* 157, 24–33.
- Colwell, J.E., Gulbis, A.A.S., Horanyi, M., Robertson, S., 2005. Dust transport in photoelectron layers and the formation of dust ponds on Eros. *Icarus* 175, 159–169.
- Culling, E.H., 1960. Analytical theory of erosion. *J. Geol.* 68, 336–344.
- Dainty, M.A., Toksöz, M.N., Anderson, K.R., Pines, P.J., Nakamura, Y., Latham, G., 1974. Seismic scattering and shallow structure of the Moon in Oceanus Procellarum. *Moon* 9, 11–29.
- Duennebier, F., Sutton, G.H., 1974. Meteoroid impacts recorded by the short-period component of Apollo 14 lunar passive seismic station. *J. Geophys. Res.* 79 (18), 4365–4374.
- Farinella, P., Vokrouhlicky, D., Hartmann, W.K., 1998. Erratum: Meteorite delivery via Yarkovsky orbital drift. *Icarus* 132 (2), 378–387.
- Fujiwara, A., 1991. Stickney-forming impact on Phobos—Crater shape and induced stress distribution. *Icarus* 89, 384–391.
- Gault, D.E., Heitowit, E.D., 1963. The partition of energy for hypervelocity impact craters formed in rock. In: *Proc. Sixth Hypervelocity Impact Symposium*, vol. 2, pp. 419–456.
- Gault, D.E., Hoerz, F., Brownlee, J.B., an Hartung, D.E., 1974. Mixing of the lunar regolith. *Proc. Lunar Sci. Conf.* 5, 2365–2386.
- Greenberg, R., Nolan, M.C., Botke, W.F., Kolvoord, R.A., Veverka, J., 1994. Collisional history of Gaspra. *Icarus* 107, 84–97.
- Greenberg, R., Botke, W.F., Nolan, M., Geissler, P., Petit, J., Durda, D.D., Asphaug, E., Head, J., 1996. Collisional and dynamical history of Ida. *Icarus* 120, 106–118.
- Holsapple, K.A., 1993. The scaling of impact processes in planetary sciences. *Annu. Rev. Earth Planet. Sci.* 21, 333–373.
- Houston, W.N., Moriwaki, Y., Chang, C.S., 1973. Downslope movement of lunar soil and rock caused by meteor impact. In: *Proc. of the 4th Lunar Science Conf. Geochim. Cosmochim. Acta* 3 (Suppl. 4), 2425–2435.
- Ivanov, B.A., 1991. Mechanical consequences of impact formed crater Stickney on Phobos. *Lunar Planet. Sci. Conf. Abstr.* 8, 619–620.
- Ivanov, B.A., Neukum, G., Botke, W.F., Hartmann, W.K., 2002. The comparison of size-frequency distributions of impact craters and asteroids and the planetary cratering rate. In: Botke Jr., W.F., Cellino, A., Paolicchi, P., Binzel, R.P. (Eds.), *Asteroids III*. Univ. of Arizona Press, Tucson, pp. 89–101.
- Jibson, R.W., Harp, E.L., Michael, J.A., 1998. A method for producing digital probabilistic seismic landslide hazard maps: An example from the Los Angeles, California, area. *Tech. Rep. United States Geological Survey*, Flagstaff, AZ.
- Kanamori, H., Given, J.W., 1983. Lamb pulse observed in nature. *Geophys. Res. Lett.* 10, 373–376.
- Kreyszig, E., 1993. *Advanced Engineering Mathematics*. Wiley, New York.
- Lambe, T.W., Whitman, R.V., 1979. *Soil Mechanics*, SI ed. Wiley, New York.
- Latham, G., McDonald, W.G., Moore, H.J., 1968. Missile impacts as sources of seismic energy on the Moon. *Science* 168, 242–245.
- Latham, G.V., Ewing, M., Press, F., Sutton, G., Dorman, J., Nakamura, Y., Toksöz, N., Wiggins, R., Derr, J., Duennebier, F., 1970. Passive seismic experiment. *Science* 167, 455–457.
- Lay, T., Wallace, T.C., 1995. *Modern Global Seismology*. Academic Press, San Diego.
- Lee, P., 1996. Dust levitation on asteroids. *Icarus* 124, 181–194.
- McGarr, A., Latham, G.V., Gault, D.E., 1969. Meteoroid impacts as sources of seismicity on the Moon. *J. Geophys. Res.* 74 (13), 5981–5994.
- Melosh, H.J., 1979. Acoustic fluidization—A new geologic process. *J. Geophys. Res.* 84 (13), 7513–7520.
- Melosh, H.J., 1989. *Impact Cratering: A Geologic Process*. Oxford Univ. Press, New York.
- Melosh, H.J., Ryan, E.V., 1997. NOTE: Asteroids: Shattered but not disperse. *Icarus* 129, 562–564.
- Michel, P., Farinella, P., Froeschlé, C., 1998. Dynamics of Eros. *Astron. J.* 116, 2023–2031.
- Nakamura, Y., 1976. Seismic energy transmission in the lunar surface zone determined from signals generated by movement of lunar rovers. *Bull. Seismol. Soc. Am.* 66, 593–606.
- Nash, D.B., 1980. Morphologic dating of degraded normal fault scarps. *J. Geol.* 88, 353–360.
- Newmark, N.M., 1965. Effects of earthquakes on dams and embankments, fifth Rankine lecture. *Geotechnique* 15, 139–160.
- Nolan, M.C., Asphaug, E., Greenberg, R., 1992. Numerical simulation of impacts on small asteroids. *Bull. Am. Astron. Soc.* 24, 959.
- Nolan, M.C., Asphaug, E., Melosh, H.J., Greenberg, R., 1996. Impact craters on asteroids: Does gravity or strength control their size? *Icarus* 124, 359–371.
- O'Brien, D.P., Greenberg, R., 2005. The collisional and dynamical evolution of the Main Belt and NEA size distributions. *Icarus*. In press.
- Pandit, B.I., Tozer, D.C., 1970. Anomalous propagation of elastic energy within the Moon. *Nature* 226, 335.
- Press, W.H., Teukolsky, S.A., Vetterling, W.T., Flannery, B.P., 1992. *Numerical Recipes in FORTRAN 77*. Cambridge Univ. Press, Cambridge.
- Prockter, L., Thomas, P., Robinson, M., Joseph, J., Milne, A., Bussey, B., Veverka, J., Cheng, A., 2002. Surface expressions of structural features on Eros. *Icarus* 155, 75–93.
- Richards, P.G., 1979. Elementary solutions to Lamb's problem for a point source and their relevance to three-dimensional studies of spontaneous crack propagation. *Bull. Seismol. Soc. Am.* 69, 947–956.

- Richardson, D.C., Leinhardt, Z.M., Melosh, H.J., Bottke, W.F., Asphaug, E., 2002. Gravitational aggregates: Evidence and evolution. In: Bottke Jr., W.F., Cellino, A., Paolicchi, P., Binzel, R.P. (Eds.), *Asteroids III*. Univ. of Arizona Press, Tucson, pp. 501–515.
- Richardson, J.E., Melosh, H.J., Greenberg, R., 2004. Impact-induced seismic activity on Asteroid 433 Eros: A surface modification process. *Science* 306, 1526–1529.
- Robinson, M.S., Thomas, P.C., Veverka, J., Murchie, S.L., Caricich, B., 2001. The nature of ponded deposits on 433 Eros. *Nature* 413, 396–400.
- Robinson, M.S., Thomas, P.C., Veverka, J., Murchie, S.L., Wilcox, B.B., 2002. The geology of 433 Eros. *Meteor. Planet. Sci.* 37, 1651–1684.
- Roering, J.J., Kirchner, J.W., Dietrich, W.E., 1999. Evidence for non-linear, diffusive sediment transport on hillslopes and implications for landscape morphology. *Water Resour. Res.* 35, 853–870.
- Schultz, P.H., Gault, D.E., 1975a. Seismic effects from major basin formations on the Moon and Mercury. *Moon* 12, 159–177.
- Schultz, P.H., Gault, D.E., 1975b. Seismically induced modification of lunar surface features. *Proc. Lunar Sci. Conf.* 6, 2845–2862.
- Schultz, P.H., Gault, D., Greeley, R., 1977. Interpreting statistics of small lunar craters. *Proc. Lunar Sci. Conf.* 8, 3539–3564.
- Shoemaker, E.M., Hait, M.H., Swann, G.A., Schleicher, D.L., Schaber, G.G., Sutton, R.L., Dahlem, D.H., Goddard, E.N., Waters, A.C., 1970. Origin of the lunar regolith at Tranquillity Base. *Geochim. Cosmochim. Acta Suppl.* 1, 2399.
- Soderblom, L.A., 1970. A model for small-impact erosion applied to the lunar surface. *J. Geophys. Res.* 75 (14), 2655–2661.
- Sullivan, R., Greeley, R., Pappalardo, R., Asphaug, E., Moore, J.M., Morrison, D., Belton, M.J.S., Carr, M., Chapman, C.R., Geissler, P., Greenberg, R., Granahan, J., Head, J.W., Kirk, R., McEwen, A., Lee, P., Thomas, P.C., Veverka, J., 1996. Geology of 243 Ida. *Icarus* 120, 119–139.
- Thomas, P.C., Joseph, J., Carcich, B., Veverka, J., Clark, B.E., Bell, J.F., Byrd, A.W., Chomko, R., Robinson, M., Murchie, S., Prockter, L., Cheng, A., Izenberg, N., Malin, M., Chapman, C., McFadden, L.A., Kirk, R., Gaffey, M., Lucey, P.G., 2002. Eros: Shape, topography, and slope processes. *Icarus* 155, 18–37.
- Titley, S.R., 1966. Seismic energy as an agent of morphologic modification on the Moon. Tech. Rep. United States Geological Survey, Flagstaff, AZ.
- Tittmann, B.R., 1977. Lunar rock Q in 3000–5000 range achieved in laboratory. *R. Soc. London Philos. Trans. Ser. A* 285, 475–479.
- Tittmann, B.R., Clark, V.A., Spencer, T.W., 1980. Compressive strength, seismic Q, and elastic modulus. *Proc. Lunar Sci. Conf.* 11, 1815–1823.
- Toksoz, M.N., Dainty, A.M., Solomon, S.C., Anderson, K.R., 1974. Structure of the Moon. *Rev. Geophys. Space Phys.* 12, 539–567.
- Veverka, J., Thomas, P.C., Robinson, M., Murchie, S., Chapman, C., Bell, M., Harch, A., Merline, W.J., Bell, J.F., Bussey, B., Carcich, B., Cheng, A., Clark, B., Domingue, D., Dunham, D., Farquhar, R., Gaffey, M.J., Hawkins, E., Izenberg, N., Joseph, J., Kirk, R., Li, H., Lucey, P., Malin, M., McFadden, L., Miller, J.K., Owen, W.M., Peterson, C., Prockter, L., Warren, J., Wellnitz, D., Williams, B.G., Yeomans, D.K., 2001. Imaging of small-scale features on 433 Eros from NEAR: Evidence for a complex regolith. *Science* 292, 484–488.
- Walker, J.D., Huebner, W.F., 2004. Loading sources for seismological investigations of near-Earth objects. *Adv. Space Res.* 33, 1564–1569.
- Wilkison, S.L., Robinson, M.S., Thomas, P.C., Veverka, J., McCoy, T.J., Murchie, S.L., Prockter, L.M., Yeomans, D.K., 2002. An estimate of Eros's porosity and implications for internal structure. *Icarus* 155, 94–103.
- Woronow, A., 1978. A general cratering-history model and its implications for the lunar highlands. *Icarus* 34, 76–88.
- Yeomans, D.K., Antreasian, P.G., Barriot, J.-P., Chesley, S.R., Dunham, D.W., Farquhar, R.W., Giorgini, J.D., Helfrich, C.E., Konopliv, A.S., McAdams, J.V., Miller, J.K., Owen, W.M., Scheeres, D.J., Thomas, P.C., Veverka, J., Williams, B.G., 2000. Radio science results during the NEAR–Shoemaker spacecraft rendezvous with Eros. *Science* 289, 2085–2088.
- Zuber, M.T., Smith, D.E., Cheng, A.F., Garvin, J.B., Aharonson, O., Cole, T.D., Dunn, P.J., Guo, Y., Lemoine, F.G., Neumann, G.A., Rowlands, D.D., Torrence, M.H., 2000. The shape of 433 Eros from the NEAR–Shoemaker laser rangefinder. *Science* 289, 2097–2101.